



Precise control of water and wastewater treatment systems with non-ideal heterogeneous mixing models and high-fidelity sensing

Tianbao Wang^{a,1}, Chenyu Wang^{b,1}, Zhiheng Xu^a, Can Cui^c, Xingyu Wang^a, Zoe Demitrack^a, Zheqin Dai^a, Amvrossios Bagtzoglou^a, Matthew D. Stuber^{b,*}, Baikun Li^{a,*}

^a Department of Civil & Environmental Engineering, University of Connecticut, Storrs, CT 06269, United States

^b Department of Chemical and Biomolecular Engineering, University of Connecticut, Storrs, CT 06269, United States

^c Department of Material Science and Engineering, University of Connecticut, Storrs, CT 06269, United States

ARTICLE INFO

Keywords:

Non-ideal heterogeneous mixing models
Precise Control
Heterogeneity profiling
High-accuracy sensing
Global optimization
Water/Wastewater treatment systems

ABSTRACT

Non-ideal heterogeneous mixing models are developed and incorporated within advanced closed-loop control strategies utilizing high-resolution sensing to maximize the resiliency and minimize the energy consumption of water treatment processes with intelligent model-based decision-making approaches. The proposed non-ideal heterogeneous mixing models capture continuity (heat and mass conservation), yet are extremely simple with few parameters, so they lend themselves to fast online prediction (with extrapolation capabilities) and regular recalibration. Further, they are more accurate than computational fluid dynamics (CFD) (60% less error) and symbolic regression data-driven models (73% less error). Real-time high-resolution sensor data are collected for observing spatiotemporal responses of state variables (conductivity, pH, and temperature) to transient influent shocks. Deterministic global dynamic optimization is used for training and recalibration of the non-ideal heterogeneous mixing models to guarantee the best-possible fits to the sensor data. The models are then deployed within standard model-predictive control and two economic model-predictive control strategies to demonstrate model-based decision-making for disturbance rejection and optimal operation of aeration in a continuous flow nitrification system utilizing high-resolution sensor data from several spatial positions. The new technology platform, consisting of high-resolution sensors, non-ideal heterogeneous mixing modeling, deterministic global dynamic optimization, and model-predictive control, offers superior performance over current approaches in water and wastewater treatment processes.

1. Introduction

The urgent demand for enhanced water quality, high resiliency, high treatment efficiency, low costs, and environmentally-friendly operations have promoted the development of model-based decision-making and control strategies in water and wastewater treatment plants (WTPs and WWTPs) [1–4]. The prerequisite to an effective control system is the ability to measure important water quality information (e.g., conductivity, pH, temperature, etc.) by high-fidelity sensing technologies, that can then be used to build reliable predictive models as well as for real-time state measurement. Though classical, purely physics-based unit operations models (e.g., activated sludge model (ASM) [5–8], a hydraulic model [9], and a sedimentation tank model [1,10]) have been used extensively in the past, they have their limitations. For example,

building models is time-consuming and some necessary parameters (e.g., cell growth rate, biomass yield) in these models are unmeasurable in WTP/WWTPs in real-time. Such variables are normally determined by offline analyses in the laboratory, causing serious time delays [1,11,12] in operator response. As a consequence, transients and spatial heterogeneity in process units go undetected, hampering efficiency improvement efforts due to an incomplete understanding of the transport processes of water quality information [13–15].

In situ data-driven approaches could overcome the existing modeling drawbacks by enabling the identification of the “black box” systems (e.g., aeration tanks) using data from the practical process under real operating conditions [16,17]. However, traditional data-driven methods in WTPs/WWTPs have two obstacles. First, some data-driven models are developed based on markedly large data acquisition and processing over

* Corresponding authors.

E-mail addresses: stuber@alum.mit.edu (M.D. Stuber), baikun.li@uconn.edu (B. Li).

¹ Tianbao Wang and Chenyu Wang share co-first authorship.

long periods. Unfortunately, in many situations only a small amount of data points have a critical influence on the system. Thus, using excess data will dilute important signals, and is unsuitable for identifying transient situations (e.g., fast chemical transport processes) [13]. The second limitation is that pure data-driven approaches are based on regression without considering physical principles, even for less complicated phenomena (e.g., dynamic neural network prediction of flow rate [18]) in WTP/WWTPs, and are therefore limited to interpolated prediction. These data-driven identification techniques may perform well for complicated systems since empirical correlations and first-principles may not accurately capture the behavior of the system due to limited information [18,19]. As a result, these models are unable to capture important fundamental mechanisms, and thus are generally less functional for further model-based control applications where extrapolative prediction is needed. Fortunately, well-understood phenomena, like heat and mass transport, can be readily and accurately modeled using first-principles.

This study explores an innovative approach to obtain high-resolution spatiotemporal data from real-time *in-situ* water quality sensors, build and validate accurate models for the measured water quality parameters, and deploy those models for precise model-based control of WTP/WWTPs. Simple non-ideal heterogeneous mixing models are developed to simulate and predict heterogeneous mass transport in WTP/WWTPs. In order to achieve visualization of the whole system, the transport characteristics of three important attributes of water quality (conductivity [20], pH [21], and temperature [22]) are elucidated with only a small volume of data collected within short periods (e.g., 2–10 min). These models are then utilized within a technology platform for the precise control of WTP/WWTPs using several different control strategies and architectures, including conventional and economic model-predictive control for improving energy and chemical-use efficiency in WTP/WWTPs.

One novel contribution of this study is that deterministic global (dynamic) optimization [23–27] is employed for better understanding the heterogeneous mixing phenomena via rigorous parameter estimation. Finding a global optimum is far more difficult than finding an arbitrary local solution; yet, a mismatch between the model and the data cannot be declared unless the best-possible fit is verified. Therefore, this approach provides additional benefits for preventing erroneously invalidating proposed mechanisms in cases where local algorithms return poor, suboptimal fits. A comparison between local and global optimal

solutions within this context is shown in Fig. 1, illustrating the conductivity profile in different positions of a tank. As shown, the sub-optimal solution obtained by a local optimization algorithm [28,29] differs significantly from a global solution. The advantages of the developed non-ideal heterogeneous mixing models are demonstrated through their straightforward, interpretable mathematical expressions able to achieve a better fit as compared to both pure data-driven symbolic regression machine learning approaches using Eureqa® (Version 1.24.0 (build 9367), DataRobot) [66] and a pure computational fluid dynamics (CFD) approach. Furthermore, the predictive capabilities are also validated by additional experimental datasets of chemical species (e.g., KCl, MgSO₄, NaOH), verifying that provided models could work for model-predictive control (MPC) in a broad spectrum of operating scenarios.

This paper is organized as follows. In Section 2, the Materials and Methods used in this study are presented. Summarily, the experimental methods are discussed as well as the model development, rigorous parameter estimation, and the control architectures for precise control of WWTPs. Section 3 contains the Results and Discussion, whereby the performance of the non-ideal heterogeneous mixing models is demonstrated, as are the control architectures for precise control of WWTPs. Conclusions follow in Section 4.

2. Materials and methods

Fig. 2 illustrates at a high level, the methods used in this study. In Fig. 2a, we illustrate the experimental methods for data acquisition as discussed in Section 2.1. Fig. 2b illustrates the overall schematics of calibration (detailed in Section 2.3) and advanced control strategies of WTP/WWTPs developed in this work (detailed in Section 2.4). Fig. 2c illustrates a continuous flow nitrification reactor representative of a commercial WWTP operation (detailed in Section 2.4).

2.1. Non-ideal mixing profiling using Milli-Electrode array (MEA) sensors

All three types of MEA sensors (each size: 2 cm × 0.5 cm) targeting three water quality parameters (conductivity, pH, and temperature) were precisely printed on Kapton polyimide film (FPC, thickness: 127 μm, American Durafilm) by a Dimatix Materials Printer (ModelDMP-2800, FUJIFILM Dimatix, Inc.) as previously reported [30,31]. Three assemblies of MEA sensors of each were deployed at three locations (high position: 40 mm below the water surface; middle position: 85 mm below the water surface; low position: 130 mm below the water surface) of a batch stirred reactor (diameter: 62 mm, height: 180 mm) (Fig. 2a) to accurately profile the whole reactor.

The sensor readings were recorded by a multi-channel potentiostat (1040C 8-channel potentiostat, CH Instruments, Inc.) every 2 s. It took 10 min to reach steady-state operation with continuous stirring with a rotation rate of 50 RPM. Then, different species (chemicals purchased from Fisher Science, Co.) were individually injected into the reactor to simulate transient shocks. Specifically, for conductivity shocks, 200 μL (100 g/L) sodium chloride was injected into the reactor on the three locations (high, middle, and low) respectively. For pH shock, 200 μL (1 M) potassium hydroxide solution mixed in 2 mg/L sodium chloride solution (pH = 14) was injected into the reactor (initial pH: 7.22) on the three locations (high, middle, and low) in turn. For temperature shock, the water solution in the reactor (initial temperature: 18.5 ± 0.12 °C, room temperature) was placed on a heating plate that was heated to 200 °C within 30 s and then shut off. All shock tests were conducted with three repeated experiments and the average values were calculated to compensate for the uncertainty in experimental procedure. Validation tests were carried out under the same conditions, except the shock substance was changed to 200 μL KCl solution (100 g/L) and 200 μL MgSO₄ solution (100 g/L) for conductivity model validation, and to 200 μL NaOH solution (1 M) for pH shock validation. These shock substances were only injected into the high zone of the reactor.

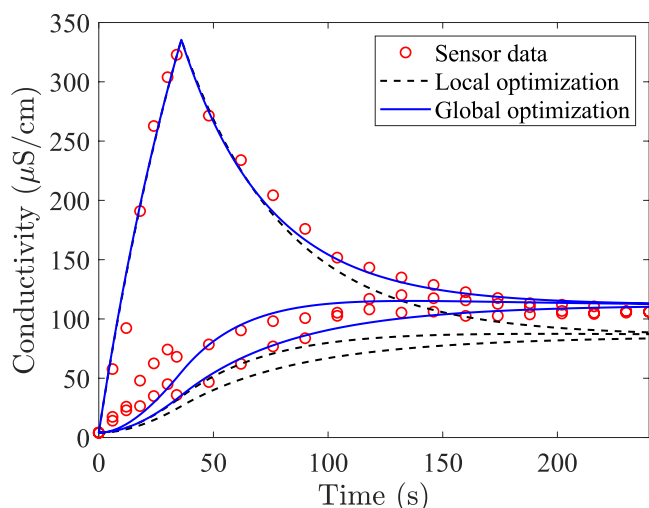


Fig. 1. Comparison of the conductivity profiles using local optimization (black dashed lines) and global optimization (blue solid lines) are presented in this figure. The conductivity model is a dynamic system under a pulse response. The three trajectories represent profiles in three different positions of the tank (high, middle, and low zones).

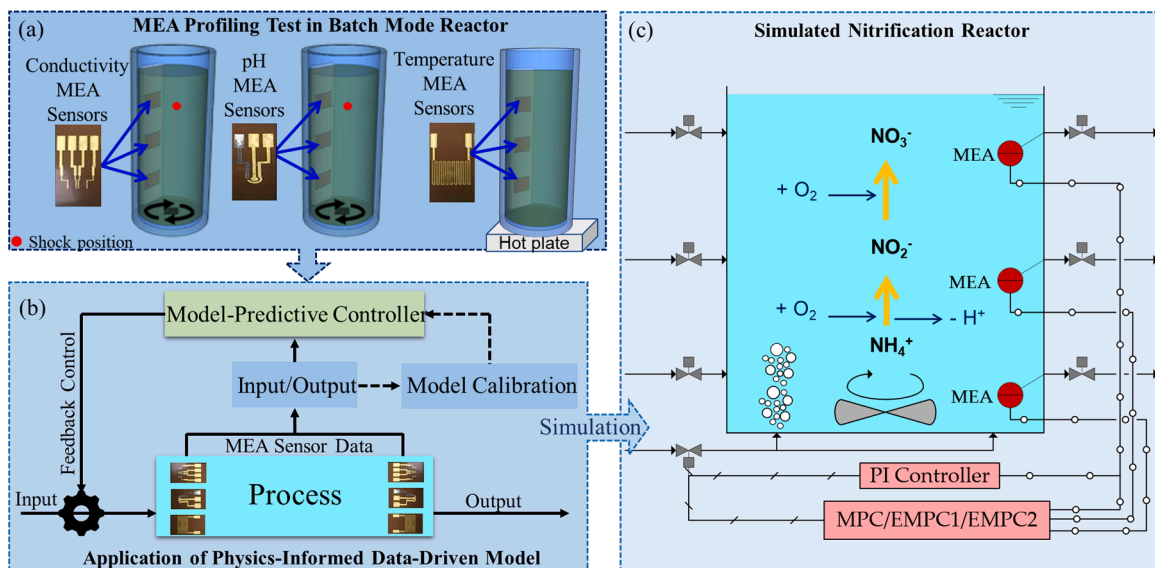


Fig. 2. (a) The experimental setup is illustrated for profiling tests along the batch reactor depth under the conductivity shock, pH shock, and temperature shock measured by the MEA sensors. (b) A schematic of the application of non-ideal heterogeneous mixing models in an online model-predictive controller (MPC) system is illustrated. (c) The simulated continuous stirred tank nitrification reactor is illustrated with inflows and outflows located at high, middle, and low zones, and a PI controller or MPC for controlling aeration.

2.2. Non-ideal mixing model development

Non-ideal heterogeneous mixing models were developed to simulate conductivity, pH, and heat transport processes inside the reactor. Specifically, to capture the spatiotemporal heterogeneity of the conductivity and pH profiles, the tank reactor was modeled using multiple regions with interchange [32]. The models were established based on heat and mass conservation that characterize the observed physical phenomena. These models were then used within a continuous flow nitrification

reactor model for precise control.

2.2.1. Conductivity mixing model

In this section, non-ideal mixing models are developed to capture the conductivity heterogeneity with respect to sensor measurements at different positions. The tank was partitioned into different nominal zones based on the positions of three MEA conductivity sensors (Fig. 3a-c). The high, middle, and low zones represent the regions corresponding with the sensor assigned within that location. The mixing zone

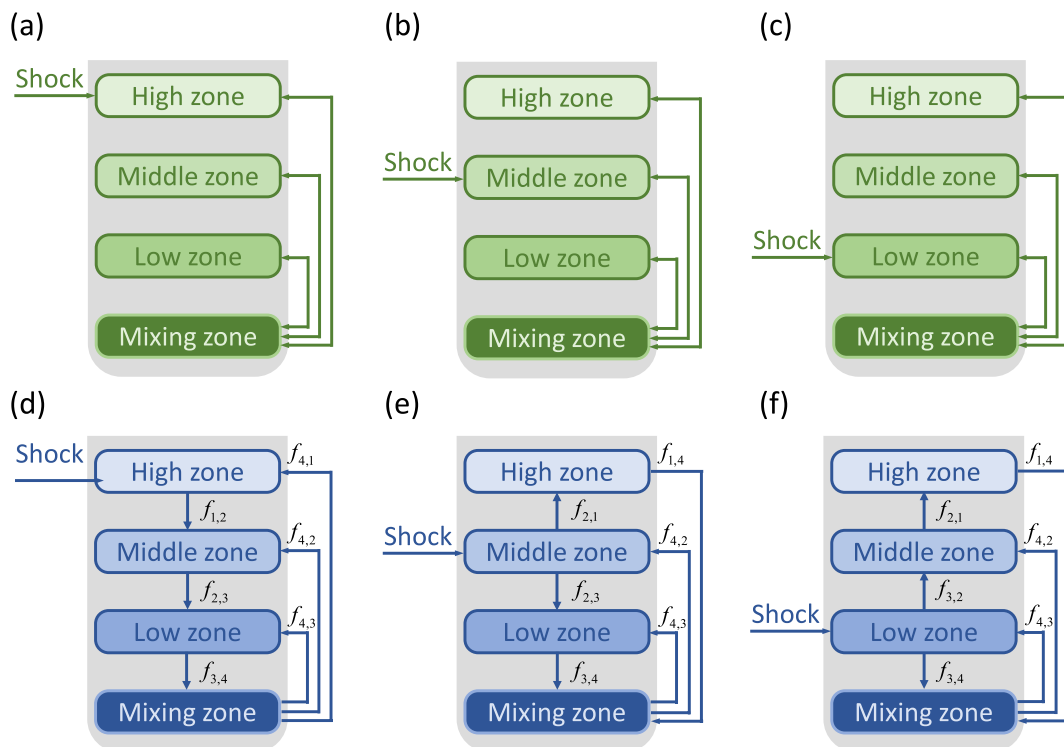


Fig. 3. Schematics of the NaCl electrolyte conductivity transport model are illustrated for shocks injected at (a) high zone, (b) middle zone, and (c) low zone, and the hydroxide ion transport model with shocks injected at (d) high zone, (e) middle zone, and (f) low zone.

represents the region where the stirrer resides on the bottom of the reactor. The dominant mechanism for mixing is forced convection, which is significantly greater than the diffusive mixing between each zone [33]. Thus, it was assumed that the stirring power dominates the mass transfer in the reactor under fast stirring, while the diffusion between adjacent zones could be neglected. The Reynolds number for the conductivity experiments is $Re = 1198.76$ (calculation process is introduced in Section 3.1), which coincides with the laminar/turbulent transition region in an agitated cylindrical tank. The ion transport between the mixing zone and each sensor zone is defined as:

$$\begin{aligned} \frac{dC_i}{dt} &= \frac{1}{4V}k_i(C_0 + C_4 - C_i), \quad i = 1, 2, 3, \\ \frac{dC_4}{dt} &= \frac{1}{4V}k_4(C_1 + C_2 + C_3 - 3C_4) \end{aligned} \quad (1)$$

Here, C_i represents the electrolytic conductivity ($\mu\text{S}/\text{cm}$) of the solutions in each zone ($i = 1, 2, 3, 4$), V is the volume of the reactor (0.38 L), and k_i is a volumetric mass transfer coefficient (L/s) that represents the rate of forced convective mass transfer between the mixing zone and zone i . C_0 represents the inlet conductivity in the corresponding zone, which is equal to C_v (shock conductivity, $\mu\text{S}/\text{cm}$) in the zone with the injected shock during the injection period (i.e., the time duration for which the conductivity in the injection zone rises to a peak) or zero for other cases (note: nomenclature of all mathematical symbols, subscripts, and superscripts appearing in equations are listed in Table S1 of the supplementary information (SI)). Three series of experiments were performed, where a high-concentration shock solution was injected into each high, middle, and low zones. The corresponding model was then developed based on the injection position.

2.2.2. pH mixing model

In this section, non-ideal mixing models are established to capture pH heterogeneity within the high, middle, and low zones of the reactor. As the solute, hydroxide ions exhibit anomalously high apparent mobilities in aqueous solutions [34,35]. Previous studies found that this anomalous transport behavior at the molecular level [36] was attributed to continuous interconversion between a hydration complex of hydroxide ions and water molecules. Thereby, apart from forced convection and diffusive transport, the hydroxide ions undergo electrochemical interactions with water molecules, grabbing protons from adjacent water molecules to generate hydroxide ion clusters at adjacent new sites. The superficial transfer coefficients are introduced to represent these multifactorial interactions between each zone (Fig. 3d-3f). Three independent experiments were conducted with shocks injected at high, middle, and low injection positions. Different models are developed based on the corresponding transfer mechanism, as illustrated in Fig. 3d-3f. For the KOH shock high-zone injection case, the model is established as:

$$\begin{aligned} \frac{dH_1}{dt} &= \frac{1}{v_1V}(H_0 + \kappa_1H_4 - \kappa_1H_1), \\ \frac{dH_2}{dt} &= \frac{1}{v_2V}(\kappa_1H_1 + \kappa_2H_4 - (\kappa_1 + \kappa_2)H_2), \\ \frac{dH_3}{dt} &= \frac{1}{v_3V}((\kappa_1 + \kappa_2)H_2 + \kappa_3H_4 - (\kappa_1 + \kappa_2 + \kappa_3)H_3), \\ \frac{dH_4}{dt} &= \frac{1}{(1 - v_1 - v_2 - v_3)V}((\kappa_1 + \kappa_2 + \kappa_3)H_3 - (\kappa_1 + \kappa_2 + \kappa_3)H_4) \end{aligned}$$

In this model, H_i represents the pH corresponding to each zone ($i = 1, 2, 3, 4$) in the reactor, v_i is the volume fraction of zone i , and κ_i is the superficial transport coefficient, indicating the "flow rate" of OH^- between adjacent zones that accounts for both reaction and convection transport (L/s). H_0 represents the input in the high zone which is equal to H_v (shock pH) during the injection period (0–8 s) and is equal to zero for the remaining process. The details and the development of pH

models for middle and low zone injection cases are summarized in Section S1 of the SI.

2.2.3. Temperature profiling model

Heat transport was assumed to be significantly slower than fluid transport [33], indicating that the transport process of heat in each sensor zone should be the same (as shown in Fig S1 of the SI). Thus, only a single equation is required to accurately model the bulk fluid temperature based on the energy balance for the batch system [37]:

$$\frac{dT}{dt} = -\frac{UA_c}{V\rho C_p}(T - T_c).$$

Here, T is the temperature of the water solution ($^{\circ}\text{C}$) and A_c is the cross-sectional area of the cylindrical container (m^2) across which heat transfer is occurring. ρ and C_p are respectively the density (kg/m^3) and heat capacity ($\text{kJ}/(\text{kg}\cdot^{\circ}\text{C})$) of the water ($\rho = 998.19, C_p = 4.18$). T_c is the temperature of the inner face of the bottom of the reactor and U is the overall heat transfer coefficient of the system ($\text{kW}/(\text{m}^2\cdot^{\circ}\text{C})$). The full details for the development of the temperature model are presented in Section S2 in the SI.

2.3. Parameter estimation and model validation using global dynamic optimization

Rigorous deterministic global optimization was used to determine the uncertain parameters for validation of optimal mixing models to capture the mixing dynamics for the three targeted properties (e.g., conductivity, pH, and temperature). The general form of the global dynamic optimization problem is defined as:

$$\begin{aligned} \min_{\mathbf{p} \in \Pi \subset \mathbb{R}^{n_p}} & \phi(\mathbf{x}(\mathbf{p}, t_1), \dots, \mathbf{x}(\mathbf{p}, t_{N_t}), \mathbf{p}) \\ \text{s.t.} & \dot{\mathbf{x}}(\mathbf{p}, t) = \mathbf{f}(\mathbf{x}(\mathbf{p}, t), \mathbf{p}, t), \quad \forall t \in I = [t_0, t_f] \\ & \mathbf{x}(\mathbf{p}, t_0) = \mathbf{x}_0(\mathbf{p}). \end{aligned} \quad (2)$$

In this formulation, ϕ is the objective function formulated as the sum of squared error (SSE) between the model and the experimental data at specific discrete time points t_1, \dots, t_{N_t} , corresponding with the experimental data, for each zone in the tank. \mathbf{x} is the generic state variable vector which represents $\mathbf{C} = (C_1, C_2, C_3, C_4)$ for the conductivity model, $\mathbf{H} = (H_1, H_2, H_3, H_4)$ for the pH model (H_1, H_2, H_3 , and H_4 represent the pH value in the corresponding zones), and T for the heat transfer model. \mathbf{p} is the uncertain parameter vector requiring estimation by optimization, which belongs to the parameter set $\Pi \subset \mathbb{R}^{n_p}$. \mathbf{x}_0 is the initial condition vector for \mathbf{x} at $t = t_0$. The optimization problem is nonconvex and constrained by a system of ordinary differential equation (ODE) initial value problems (IVPs). The specific optimization formulations for conductivity and pH mixing models are summarized in Section S3 of the SI.

There has been active development of novel deterministic methods for solving eq(2) to guaranteed global optimality [25,38–41]. In this study, for conductivity and pH models, the nonlinearity comes from the bilinear terms of the system of ODEs. To solve the parameter estimation problems for these models, the models were reformulated into a system of nonlinear algebraic equations using an explicit Euler discretization and accounted for as equality constraints. As a result, the bilinear terms become recursively multiplied, resulting in the feasible set being nonconvex. The ANTIGONE v1.0 solver [42] in GAMS v24.7.4 [43] was used to solve these parameter estimation problems to guarantee global optimality (absolute stopping tolerance is set to 0; relative stopping tolerance is set to 0.1; absolute feasibility tolerance is set to 1E-6). All global optimization results were obtained within 1.5 h, which is important for applications in real-time MPC of WTPs/WWTPs with a much longer residence time. The analytical expression for the temperature model was derived and applied within the global optimization formulation (Section S4 in the SI). The global optimization problem for the temperature model was solved using the EAGO v0.2.1 solver (EAGO).

jl) [65] in the Julia programming language [44] via the JuMP v0.18 modeling language (JuMP.jl) [45]. The global results for the temperature model could be obtained within 2 min, which is appropriate for prompt temperature control in WTPs/WWTPs. The wall clock times were reported for GAMS and JuMP implementations run on a personal workstation with an Intel Xeon E3-1270v5 4-core/8-thread processor at 3.60 GHz/4.00 GHz (base/turbo) frequency running Windows 10 with 32 GB of ECC memory.

2.4. Precise control of a wastewater nitrification system

The non-ideal heterogeneous mixing models for conductivity were expanded from a batch system to an unsteady pilot-scale continuous flow nitrification CSTR (1000L) to demonstrate their applicability to real WWTPs, with a controller being implemented to showcase disturbance rejection and energy saving operations (Fig. 2c). Three inlet streams continuously flow into the tank corresponding to the high, middle, and low zones. Similarly, three outlet streams continuously flow out of the tank at the corresponding zones. In addition, there is an air diffuser at the tank bottom continuously aerating for nitrification to oxidize NH_4Cl [46]. A conductivity sensor is deployed in each zone to measure the corresponding conductivity at 10 s intervals. An impeller is in the mixing zone to continuously stir the liquid inside the tank. For traditional proportional-integral (PI) control, feedback is provided from the high-zone MEA conductivity sensor and a control signal is sent to the valve on the air stream at the bottom of the vessel. For MPC and its variants, sensors in each zone are utilized for feedback.

A modified conductivity mixing model that accounts for continuous operations in this tank is established to simulate the nitrification step:

$$\begin{aligned} \frac{dC_i}{dt} &= \frac{1}{4V} (k_i(C_4 - C_i) + \dot{m}_{in,i}C_{in,i} - \dot{m}_{out,i}C_i) + R_{\text{NH}_4^+}, \quad i = 1, 2, 3, \\ \frac{dC_4}{dt} &= \frac{1}{4V} k_4(C_1 + C_2 + C_3 - 3C_4) + R_{\text{NH}_4^+}, \\ \frac{dc_o}{dt} &= r_o + k_{la}(c_o^* - c_o), \end{aligned} \quad (3)$$

where $\dot{m}_{in,i}$ and $\dot{m}_{out,i}$ are continuous inlet and outlet flow rate at zone i (L/s), respectively, $C_{in,i}$ represents the conductivity of the inlet stream at zone i ($\mu\text{S}/\text{cm}$), and $R_{\text{NH}_4^+}$ is the reaction rate law for NH_4^+ consumption measured as conductivity ($\mu\text{S}/\text{cm}/\text{s}$), c_o is the oxygen concentration (mg/L), and r_o is the oxygen consumption rate described by a reaction rate law (mg/L/s). The aeration process is modeled by the rate of mass transfer of oxygen into the reactor liquid from air bubbles $k_{la}(c_o^* - c_o)$, where k_{la} is the volumetric mass transfer coefficient (s^{-1}) [47], and c_o^* is the saturated dissolved oxygen concentration (9.1 mg/L at 20 °C) [48]. The standard oxygen transfer rate (SOTR, mg/s) is defined as $\text{SOTR} = k_{la}c_o^*V$, and represents the amount of oxygen transferred per second at 20 °C. The standard oxygen transfer efficiency (SOTE, %) refers to the ratio of oxygen in the inlet air stream dissolved in the liquid at 20 °C, given by $\text{SOTE} = \text{SOTR}/W_o$, with W_o the mass flow of oxygen in the air stream (mg/s). W_o can be calculated by an empirical formula: $W_o = 0.2967Q$, where Q is the airflow rate adjusted by the controller. The mass transfer coefficients were adjusted to construct a modified model that can account for all situations with single or multiple shocks at high,

Table 1

Input and output variables for the nitrification wastewater system with different control strategies are listed in this table.

Control system	PI control	MPC, EMPC1, EMPC2
Input variables	Q Airflow rate	Q Airflow rate
Output variables	C_1 High zone conductivity	C_1 High zone conductivity
	C_2 Middle zone conductivity	C_2 Middle zone conductivity
	C_3 Low zone conductivity	C_3 Low zone conductivity

middle, and low zones. The model development process, the detailed kinetics for the nitrification reaction, and the mechanism for airflow and transfer into the liquid are introduced in Section S4 in the SI.

A case study of removing excess NH_4Cl in a nitrification CSTR of a WWTP is simulated as shown in Fig. 2c. The input and output variables for the control system are given in Table 1. According to the standard of moderate municipal wastewater, the concentration of ammonium ions in the effluent should not exceed 30 mg N- NH_4^+/L [49]. Thus, the operating setpoint (SP) is set at 280 $\mu\text{S}/\text{cm}$ corresponding to the standard concentration. Independent numerical experiments were conducted to assess the behavior of the system under four different influent shock conditions (i-iv) and six different operating scenarios to compare the system performance with various control approaches. From $t = 2100$ s to $t = 2250$ s, influent shocks (as step disturbances) in NH_4Cl concentration were introduced in each case as: (i) $C_{in,1} = 320\mu\text{S}/\text{cm}$, (ii) $C_{in,2} = 320\mu\text{S}/\text{cm}$, (iii) $C_{in,3} = 320\mu\text{S}/\text{cm}$, (iv) $C_{in,1} = 300\mu\text{S}/\text{cm}$, $C_{in,2} = 350\mu\text{S}/\text{cm}$ and $C_{in,3} = 270\mu\text{S}/\text{cm}$.

2.4.1. Proportional-Integral (PI) control

A traditional closed-loop PI-controller was modeled and tuned for rejecting influent conductivity shocks. The PI controller only makes decisions based on feedback signals from measurements in the high zone and adjusts the mass flow rate of air entering the system. The Internal Model Control (IMC) correlations are used to tune the PI parameters at first. Then, the parameters are further adjusted manually through simulations until the closed-loop system performs as desired. The details of the PI tuning process are introduced in S3 of the SI. An experiment is performed on the system with a unit step disturbance to evaluate the control performance, the integral time-weighted absolute error (ITAE), integral time-weighted squared error (ITSE), integral absolute error (IAE) and integral squared error (ISE) are quantified with a settling time set as 1000 s, as listed in Table 2. The economic performance of the PI controller was assessed based on energy consumption and concentration disturbance rejection under the four influent shock scenarios.

2.4.2. Model predictive control (MPC)

MPC is an advanced control technique widely used in the process industries. MPC has been proposed for applications in WTPs/WWTPs to deal with the complexities from disturbances in the influent and physical and chemical phenomena [50–52]. MPC allows for tunable closed-loop response with its primary advantage being its intuition of process dynamics and capability to naturally handle multi-input/multi-output systems. In addition, compared with conventional proportional-integral-derivative (PID) control and interval model control (IMC), MPC can handle more complicated systems (e.g., time delay, nonlinearity, open-loop instability), and provide a better response with less settling time. Therefore, a multi-input MPC was designed to improve disturbance (step function) rejection in WTP/WWTPs. The core concept of MPC is to solve an optimization problem at predetermined time points k to determine a control action that best drives the system towards the SP. In this study, the control action step size δ is set as 10 s (i.e., same as for PI control). An objective function is formulated as the sum of squares of the predicted errors (differences between the SP and the model-predicted outputs) over a prediction horizon of P control action steps [53]:

$$\min_{u_k, \dots, u_{k+M-1}} \sum_{i=1}^3 \sum_{j=1}^P (\text{SP} - \hat{C}_{i,k+j})^2. \quad (4)$$

Table 2

The control performance indices quantified by a response to a step disturbance change are presented in this table. The settling time is set as 1000 s.

Performance index	ITAE	ITSE	IAE	ISE
	2.817E4	1.606E3	5.414E1	3.185

Here, u_m ($m = k, \dots, k + M - 1$) is the control variable which is equal to the airflow rate Q in this study (kg/s), SP is the setpoint ($\mu\text{S}/\text{cm}$), \hat{C}_i is the model predicted output ($\mu\text{S}/\text{cm}$) in zone i , and the subscripts indicate the sample time (k is the current sample time). P is the number of control actions in the prediction horizon ($P = 20$), and M is the number of control actions in the control horizon ($M = 3$). M control variables u_k, \dots, u_{k+M-1} are optimized at control action step k , but only the first control action u_k is implemented. Then, similarly, a new optimization problem is solved with respect to M control variables over a prediction horizon of P at step $k + 1$. The dynamic matrix control (DMC) method was used to evaluate model predicted process outputs \hat{C}_i [53]. The performance of the MPC was assessed based on energy consumption and concentration disturbance rejection under the four influent shock scenarios.

2.4.3. Economic model predictive control (EMPC)

Economic MPC (EMPC) is a method for accounting for real-time

process operations with respect to economic performance [54]. As such, EMPC can directly account for process economics in the determination of appropriate control response, and therefore is ideal for the development of next-generation WTP/WWTPs, such as real-time energy management and market-driven production [55,56]. In this study, we formulate and implement EMPC with two different objectives: one is targeted at reducing environmental discharge (EMPC1); and the other is targeted at saving energy (EMPC2). The optimization problem for EMPC1 is defined as

$$\min_{u_k, \dots, u_{k+M-1}} \sum_{i=1}^3 \sum_{j=1}^P D_{i,k+j}^2 + w \left(\sum_{i=0}^{M-1} u_{k+i} + (P - M + 1)u_{k+M-1} \right), \quad (5)$$

where D_i is the discharge from zone i ($\mu\text{S}/\text{cm}$), that can be expressed as

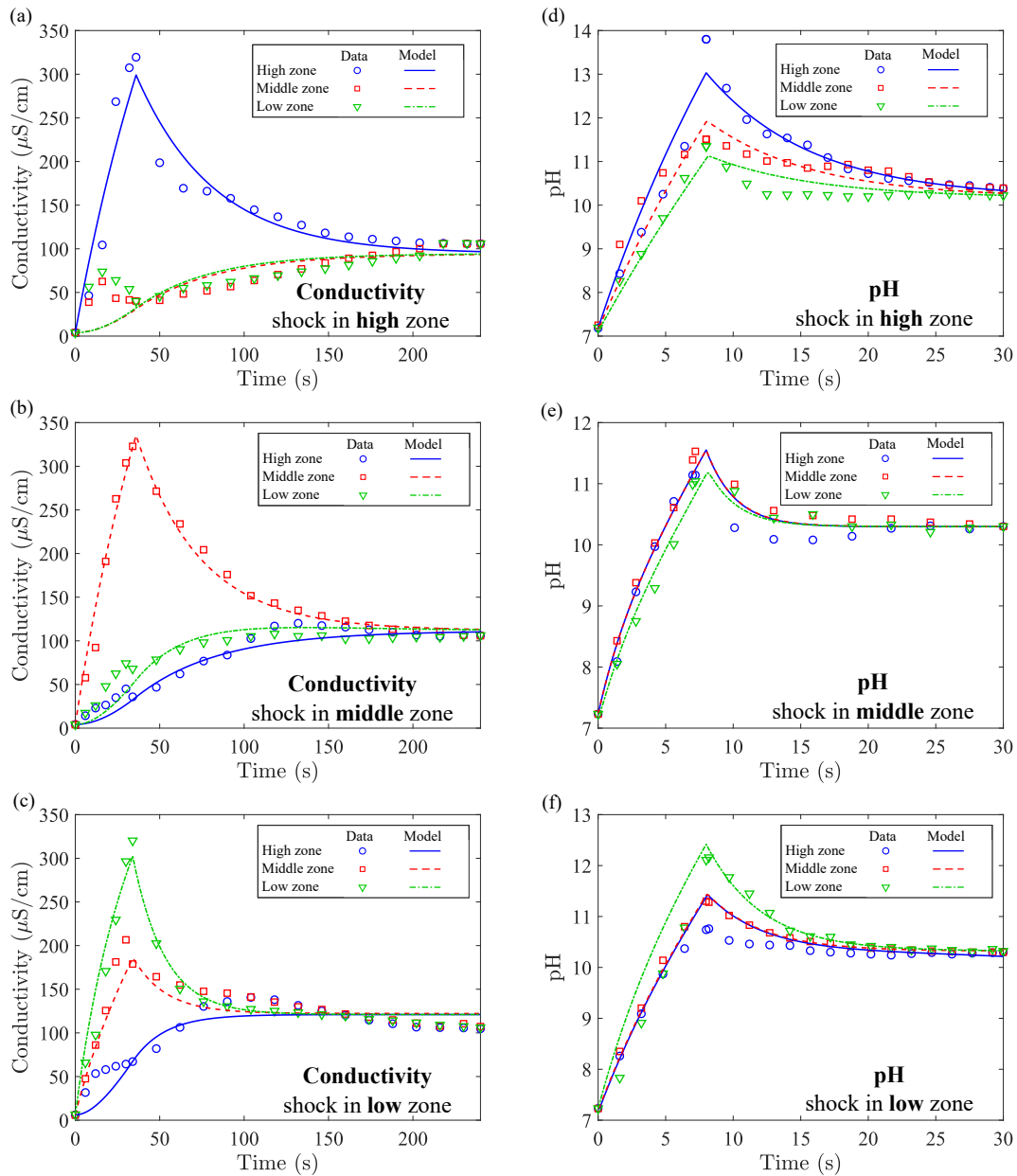


Fig. 4. Optimal conductivity profiles from the global optimization results are plotted against a subset of data for (a) the high-zone injection model, (b) middle-zone injection model, and (c) low-zone injection model. Optimal pH profiles from the global optimization results are plotted against a subset of data for (d) the high-zone injection model, (e) middle-zone injection model, and (f) low-zone injection model.

$$D_{i,k+j} = \begin{cases} \widehat{C}_{i,k+j} - SP & \text{if } \left(\widehat{C}_{i,k+j} - r \right) > 0 \\ 0 & \text{if } \left(\widehat{C}_{i,k+j} - r \right) \leq 0. \end{cases}$$

The objective is to minimize the overall discharge above the SP over the prediction horizon of P . $w \left(\sum_{i=1}^{M-1} u_{k+i} + (P-M+1)u_{k+M-1} \right)$ in eq(5) is a penalty function with respect to the control variables that guarantees the lowest oxygen consumption when the discharge is already below the SP (the penalty coefficient w is set as 0.03) and penalizes oxygen consumption when making control decisions.

EMPC2 is formulated as the constrained optimization problem:

$$\begin{aligned} \min_{u_k, \dots, u_{k+M-1}} & \delta \left(\sum_{i=0}^{M-1} u_{k+i} + (P-M+1)u_{k+M-1} \right) \\ \text{s.t.} & \widehat{C}_{i,k+j} - SP \leq 0, \quad \forall i = 1, 2, 3, \quad j = 1, \dots, M, P. \end{aligned} \quad (6)$$

We seek to minimize the overall oxygen consumption over the prediction horizon to reflect energy management during operations. The inequality constraints ensure that the conductivity profiles over the control horizon, and at the end of the prediction horizon, will be at or below the SP. The performance of each EMPC was assessed based on energy consumption and concentration disturbance rejection under the four influent shock scenarios.

3. Results and Discussion

3.1. Optimal solutions for Conductivity, pH, and temperature mixing models from parameter estimation

The global optimal solutions for parameters of conductivity and pH models are listed in Table S2 in the SI. The time costs for solving these global optimization problems are reported in Table S3 in the SI. The vast disparity in solution times for solving pH problems is due to the ‘‘curse of dimensionality’’ of deterministic global optimization [57] as the high-zone injection problem has nearly double the optimization variables of the low- and middle-zone injection problems.

The optimal conductivity profiles for different injection positions are presented in Fig. 4a-4c. Overall, the conductivity profiles fit the experimental data well, and are able to capture the transient peaks caused by shock injections. This detection of transient maximum conductivity is of great importance in applications such as preventing the damage to bacterial cells in WWTPs [58], since both nitrogen removal and phosphorus removal processes in WWTPs exhibit significant changes in the conductivity of wastewater[59]. For the high-zone injection case (Fig. 4a), it is observed that the optimal profiles in the middle and low zones do not exhibit small peaks like the data, indicating that the lower zones of the physical system receive ionic solutes from the upper zones in small amounts, which is not accounted for in the proposed model. Since the relative mismatch is quite small, no change was deemed necessary for the model. The low-zone injection profile (Fig. 4c) exhibits two conductivity peaks in the low zone and middle zone, which may be attributed to the shock injection position (low zone) being very close to the mixing zone, thus transport to the middle zone occurs rapidly. In addition, the optimal parameter C_v^* for the low-zone injection case is much smaller than the high-zone and middle-zone cases (Table S2 in the SI), indicating that the mixing force quickly dilutes the shock in the low zone due to the closest proximity to the mixing zone.

The optimal pH profiles are shown in Fig. 4d-4f. The models fit well for high-zone and middle-zone injections, while a small deviation can be observed in the high-zone pH profile in the low-zone injection model. The pH profiles for the middle-zone injection are more uniform, due to the equal probability for apparent OH⁻ transport towards the high and low sensor zones, supporting the hypothesis that the dominant driving force for apparent OH⁻ transport is the electrochemical reaction instead

of forced convection. As compared with the conductivity transport model, proton (charge) transfers much faster (~ 30 s to achieve equilibrium).

The optimal parameter values for the temperature model are $U^* = 1.9183$ and $T_c^* = 26.40$. It took 65.97 s to solve the parameter estimation problem to global optimality. Since the entire system was considered as a single stirred batch reactor (conforming to the well-mixed assumption), the optimal profile exhibits no spatial variations between each sensor zone and fits the data (Figure S1 in the SI) almost exactly. Furthermore, the convective heat transfer coefficient was also estimated, using fundamental heat transfer principles and the Nusselt number (Nu), which is the ratio of convective to conductive heat transfer across a boundary. The Nusselt number is defined as $Nu = h_l D_c / \lambda$ [33], where h_l is the convection heat transfer coefficient of the flow equivalent to the overall heat transfer coefficient U for this heat transfer model, λ is the thermal conductivity of water (W/(m²·C)) listed in Table S8 in the SI, and D_c is the characteristic length that is equal to the surface area A_c divided by the perimeter P_c of the bottom inner surface ($D_c = A_c / P_c = 0.01375$). In general, the Nusselt number can be calculated as a function of the Reynolds number (Re) and the Prandtl number (Pr). In this experiment, a cubic stirring bar ($d = 38$ mm) was used at a rotation speed (ω) of 50 RPM ($5/6$ s⁻¹). The Reynolds number is then calculated as $Re = \rho d^2 \omega / \mu = 1198.76$, indicating that it is within the transitional region for flow in a cylindrical tank ($1000 < Re < 10000$), where μ is the viscosity of water (Pa·s) listed in Table S8 in the SI. The Nusselt number (Nu) for this system can then be calculated by $Nu = 0.664 Re^{0.5} Pr^{1/3} = 44.405$ [60], where Pr is the Prandtl number of water listed in Table S8 in the SI. Finally, the heat transfer coefficient can be estimated as $h_l = \lambda Nu / D_c = 1.9289$ kW/(m²·C), which is very close (0.55% deviation) to the optimal solution U^* . Additionally, the optimal surface temperature T_c^* was higher than the observed solution temperature, which is consistent with the observed heat transfer (raising solution temperature) over the entire time horizon. The observed temperature profile shows a significant reduction in heat transfer rate as the solution temperature approaches T_c^* as the rate of temperature increase (i.e., heat transfer) slows down over this period.

3.2. Comparison of Non-ideal mixing models with pure Data-Driven models and CFD models

CFD models account for complex physical phenomena [61] and therefore are extremely computationally expensive. Typical CFD simulations of the batch reactor took 1.5 h on computers similar to the one reported previously and required excessive memory storage. Note that this computational cost does not account for the substantial time investment needed for the model setup and testing. Furthermore, CFD models once developed can rarely be adapted to new situations with new parameter values. More details about the CFD model used in this study are recorded in Section S6 in SI. The simulation of a CFD model (dashed line) under the high-conductivity high-zone shock fits well with the MEA sensor profiles (blue points) (Fig. 5a), while there was a large discrepancy between the CFD simulated result and the MEA sensor data points under the middle and low shock (Fig. 5b and 5c). This might be attributed to the simplification in CFD simulation for ion transport processes as it only considers ideal conditions and neglects some side-effects such as the difference in surface smoothness and difference in mixing ability in each compartment (high, middle, and low) of the batch reactor. For instance, the middle zone was assumed to have the weakest mixing ability leading to the lowest mass transfer effectiveness while the mass transfer effectiveness should be highest when the shock came from the low position closest to the mixing bar. In contrast, using the non-ideal mixing model, the SSE was reduced by 92.23% and 80.45% (Fig. 5). It should be noted that a CFD model that compartmentalizes the reactor in a similar manner to our simple non-ideal mixing model, is expected to perform much better. However, the development and

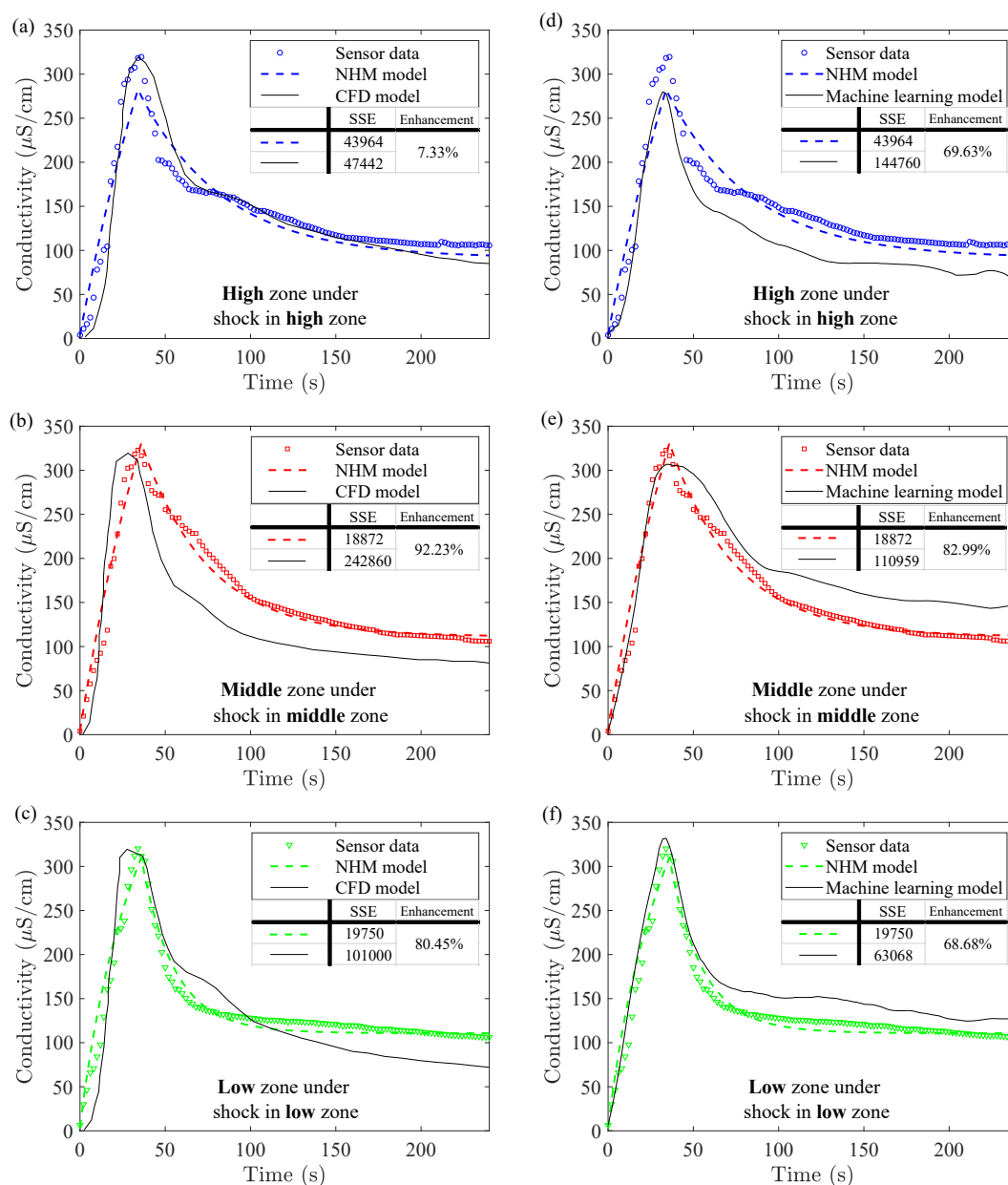


Fig. 5. Comparisons of the simulation results of the non-ideal heterogeneous mixing model (dashed line) with the fitting results of (a-c) the CFD model (solid line) and with the fitting results of (d-f) the machine learning model (solid line), are plotted for each zone corresponding with the conductivity shock injection locations. (a and d: plots of the high zone under shock injected in the high zone; b and e: plots of the middle zone under shock injected in the middle zone; c and f: plots of the low zone under shock injected in the low zone). (Note: NHM = Non-ideal heterogeneous mixing; The sensor data profile (dots) and CFD model simulation are extracted from the previous study [64]).

computational costs for such a model are considered to be prohibitive for any practical, real-time implementation and use for precise control systems.

The observed mixing trends could not be represented well by the CFD simulation under conductivity shocks (Fig. 5), let alone the fast-transient scenarios of pH with multifactorial reactions. As an example, an axisymmetric model of a pH-sensitive electrochemical field effect sensor comprising 13,650 elements was deployed to simulate a geometrical domain of 0.09 mm^2 , demonstrating that it is intractable to apply CFD models in the batch reactors used in this study (volume: 380 mL) as the grid would have to be refined by a factor of 150.

The non-ideal mixing model was also compared with a pure data-driven model from the Eureka modeling engine (DataRobot), that generates differential equations trained on the same data set. All data points were equally weighted for training (detailed settings are shown in

Figure S2 in the SI) and were integrated as black lines in Fig. 5d-f. The mean SSE (full name) values between the original sensor data and machine learning results were 144760, 110959, and 63,068 for each shock (high, middle, and low locations), respectively. In contrast, the SSE value between the original sensor data and the non-ideal mixing model's simulation results were markedly lowered by 68–83%, respectively. The poor fit of the Eureka regression models is attributed to lacking the conservation principles as a basis, so that the regression models deviate from the main trends of mass and heat transfer.

3.3. Validation and calibration of sensors and Non-ideal mixing models

The non-ideal mixing models can be easily modified to simulate conductivity or pH profiles of other solute species by calibrating the parameters. In terms of conductivity, the main transport mechanism of

ions without chemical reaction should be the same. However, the uniqueness of each ion is associated with distinct conductivity values, posing the requirement for calibrating the as-developed models to sustain accuracy under varying scenarios. To further validate the applicability of the developed non-ideal heterogeneous mixing models, additional experiments were conducted by injecting different soluble compounds (KCl, MgSO_4 and NaOH). The conductivity and pH profiles were simulated versus the experimental sensor data using the corresponding models with the parameters calibrated based on the actual experimental conditions.

For validation of the conductivity model, the original optimal parameter values (as listed in Table S2 in the SI) were used to predict the KCl and MgSO_4 conductivity profiles. The results showed that the simulated profiles using the original optimal parameter values qualitatively follow the same trends as the new data (Fig. 6a and 6c). The

reason for the significant quantitative mismatch is due to the differences in injection periods between the new and the original experiments. Since all shock injections are manual operations, the injection speeds cannot be regarded as a controllable experimental condition. The high-zone data reaches a peak much faster, indicating that the injection speeds for the KCl and MgSO_4 experiments are faster than the NaCl experiment. Apart from the injection speeds, the absolute injection quantity of different ions is another attribute leading to a mismatch. For example, though the mass concentrations of KCl and MgSO_4 (200 μL , 100 g/L) injected are the same compared with the original NaCl conductivity experiment, different ions lead to different conductivities in solution and different shock conductivity C_v . The electrical conductivities of the ionic solutions based on mass percent are listed in Table S4 in the SI. Since aqueous NaCl and KCl solutions exhibit nearly the same conductivities, the predicted KCl profile using the original NaCl injection model exhibits

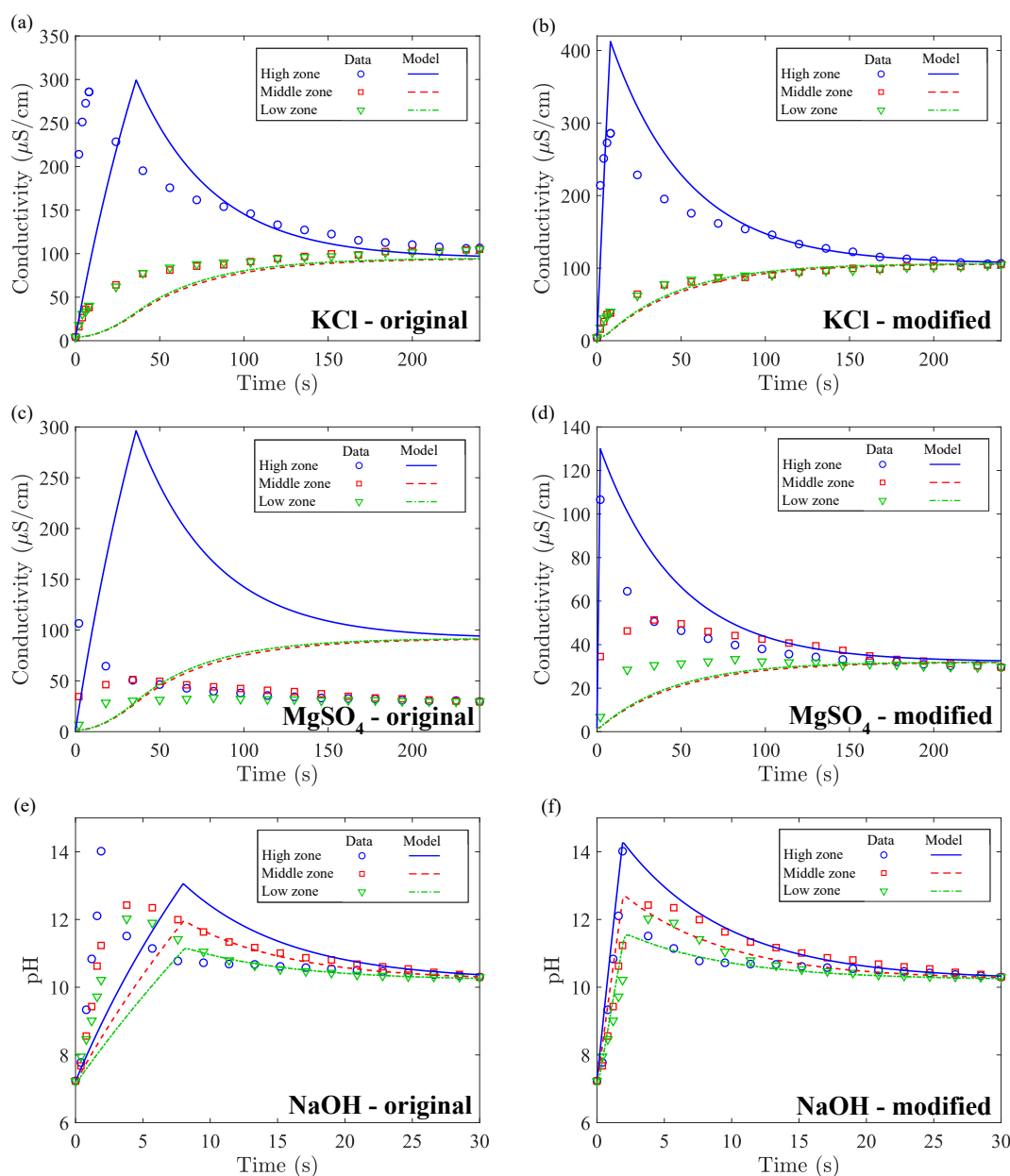


Fig. 6. The predictive simulation results are plotted for KCl conductivity profiles versus experimental data using (a) original optimal parameters and (b) modified parameters. The predictive simulation results are plotted for MgSO_4 conductivity profile versus experimental data using (c) original optimal parameters and (d) modified parameters. The predictive simulation results are plotted for NaOH pH profiles versus experimental data using (e) original optimal parameters and (f) modified parameters.

nearly the same steady-state conductivity versus the new experimental data (a). In contrast, the steady-state conductivity of the predicted MgSO_4 is around three times higher than the new experimental data (Fig. 6c). This difference is expected since MgSO_4 exhibits roughly one-third of the electrical conductivity of NaCl across the mass percentage range (Table S4 in the SI). To improve the simulation results (i.e., model prediction accuracy), a simple calibration procedure (Section S5 in the SI) was conducted without modifying the model structure, so that the underlying physical phenomena captured by the original model could be preserved. The revised conductivity profiles for KCl and MgSO_4 (Fig. 6b and 6d) exhibit substantially improved fits.

To validate the pH model for the NaOH experiment, the pH profile was simulated using the original parameters for the KOH injection case. The simulated pH profile exhibits the same qualitative behavior as the data (Fig. 6e). Again, the major mismatch is caused by the observed difference between the injection periods of the NaOH and KOH data. The time duration for the pH of the NaOH experiment to reach the peak is much shorter. Thus, the corresponding shock parameter H_v should be calibrated to mitigate this difference. The calibration process is summarized in Section S5 in the SI. The revised pH profile (Fig. 6f) exhibits a far better fit than the original simulation, where the peak pH from the model also matches the data. The profile of the high-zone pH in the short time horizon after the peak does not accurately fit the data. The probable reason is that the quasi dynamics of OH^- transport after the shock is not accurately captured by the model or the experimental errors.

3.4. Non-ideal mixing models for improved wastewater treatment with precise control

3.4.1. Simulation results for the wastewater nitrification system with Closed-Loop controls

The simulation results for each independent study are illustrated in Fig. 7. For the high-zone shock case, the PI controller begins to adjust the air valve to accelerate the airflow rate for excess ammonium removal once the disturbance occurring in the high-zone inlet flow is detected. The high-zone conductivity quickly drops below the SP, then the valve on the air stream is closed and the conductivity gradually rises towards the SP. As for middle-zone and low-zone shocks, the conductivities can still be controlled at the SP despite only using feedback readings from the high-zone sensor. The reason is that the conductivity becomes quickly mixed at around $t = 2400$ s resulting in the overall conductivity of the tank approaching the SP under control.

For comparison, the MPC simulation results are also illustrated in Fig. 7. For the high-zone shock simulation, the conductivities can be

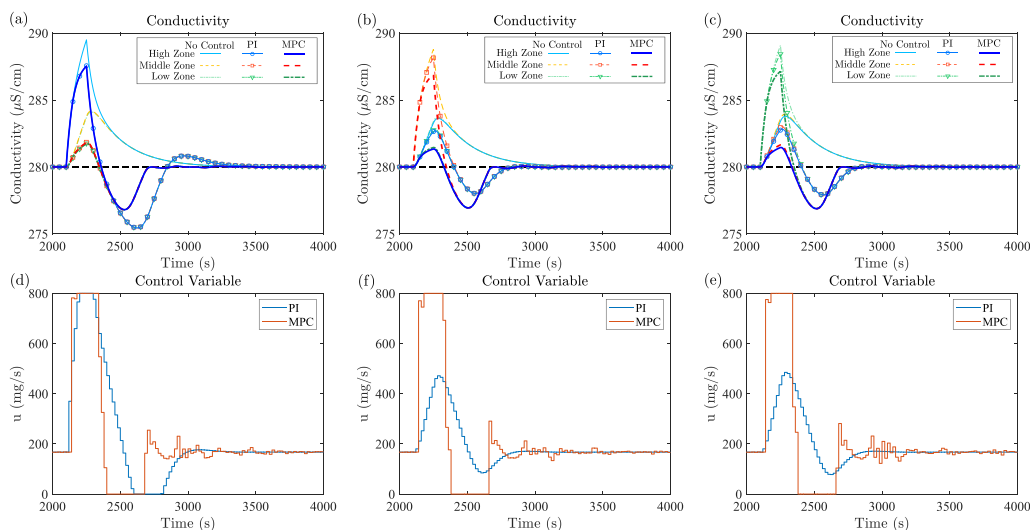


Fig. 7. The conductivity profiles are plotted for the uncontrolled, PI control, and MPC simulations for independent studies with NH_4Cl conductivity shock ($320 \mu\text{S}/\text{cm}$) continuously injected from 2100 s to 2250 s, respectively, in the (a) high, (b) middle, and (c) low zones of a continuous-flow nitrification system. The PI (blue) and MPC (orange) control actions for the (d) high-zone shock case, (e) middle-zone shock case, and (f) low-zone shock case, are presented below their corresponding conductivity profiles.

directed to the steady state at SP much faster than PI control. As indicated by the control variable, the consumption of oxygen is reduced significantly by MPC, implying substantial energy savings. Furthermore, the middle-zone and low-zone shock simulations show that with MPC, much less ammonium is discharged to the environment than with PI control. This is because multi-input MPC can account for feedback signals from all sensors, make accurate predictions of process transients using the non-ideal heterogeneous mixing models, and take appropriate action versus the PI controller that only considers feedback signals from the high-zone sensor.

3.4.2. Evaluation of treatment performance and energy savings

An open-loop controller was also simulated for each study to represent conventional and conservative operations as a reference for comparisons. Once the shock from the influent is observed ($t = 2100$ s), the operator will open the aeration valve by an amount estimated from the difference between the shock value and SP for full oxidation (u is set as $561.44 \text{ mg}/\text{s}$). After the system's fixed settling time (1000 s), the operator will adjust the valve again. In contrast, for the uncontrolled simulations, the control variable is always set at the initial value ($u_0 = 168 \text{ mg}/\text{s}$) which results in the steady-state effluent conductivity meeting the SP under steady influent conditions.

To evaluate the system's performance, the excess ammonium discharge was quantified as the area under the conductivity profiles as they go above the SP over the simulation horizon (2000 s). In addition, the energy consumption was quantified as the overall amount of air used for ammonium oxidation over the simulation horizon. The comparisons between uncontrolled, open-loop control, PI control, MPC, EMPC1, and EMPC2 cases are illustrated in Fig. 8 with the data values for these plots listed in Table S6 in the SI. The discharge quantification for each case is calculated as the percentage of the uncontrolled simulation, whereas the energy quantification is represented by the percentage of the open-loop control simulation. It is apparent from the discharge plot (Fig. 8a), that all the control strategies can greatly reduce the discharge compared with uncontrolled simulations. MPC and both EMPC strategies perform much better than PI control as less ammonium is discharged into the environment. This is especially clear for the middle- and low-zone shock studies, where MPC and EMPC account for multiple input measurements simultaneously, while PI control can only account for the high-zone measurement. Specifically, EMPC1 has the best performance for reducing discharge, coinciding with its underlying design objective. On the other hand, energy usage (Fig. 8b) under PI control, MPC, and both EMPC strategies, is reduced versus open-loop control. As for the high-zone shock injection study, MPC has the greatest advantage

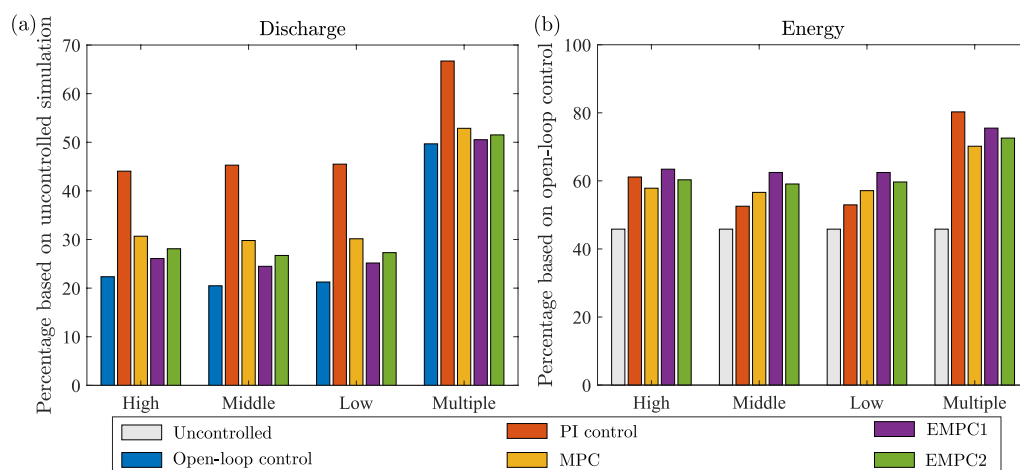


Fig. 8. (a) The overall discharge of NH_4Cl above the setpoint (SP) over the simulation horizon, is plotted for each control scenario as a percentage normalized against the uncontrolled case (the uncontrolled case is 100%). (b) The total compressed air consumption (equating to energy usage) over the simulation horizon is plotted for each control scenario as a percentage normalized against the open-loop control simulation (the open-loop control case is 100%). The labels “High”, “Middle”, “Low”, and “Multiple” represent high-zone, middle-zone, low-zone, and multiple-zone shocks, respectively. In both cases, lower percentages equate to better performance.

due to the least energy usage among other control strategies while its discharge is only slightly higher than EMPC1 and EMPC2. As for the middle- and low-zone shock studies, PI control saves the most energy, but also has the greatest discharge compared with the other strategies.

It is observed that MPC has lower energy usage compared with EMPC1 and EMPC2. EMPC1 is formulated to minimize environmental discharge and it is apparent that more energy is consumed to achieve this objective. EMPC2 is formulated to minimize air consumption with constraints on discharge, but as indicated, it still consumes slightly more energy than MPC. The reason for this behavior is that EMPC2 seeks a control setting that has the lowest energy consumption with a prerequisite to strictly satisfy the discharge constraints while MPC only minimizes the errors without any specifications on discharge.

For the multiple shocks study, barring open-loop control, PI control is apparently the worst control strategy using the most energy and resulting in the most ammonium discharge. The energy usage and discharge for MPC, EMPC1, and EMPC2 are relatively similar, and any lower discharge observed must be paid for with greater energy consumption. It is suggested that for real-world operation, control strategies should be determined based on the specific conditions of the WTP/WWTP. This is aligned with the notion of “smart plant operations,” where process control, plant-wide management, and corporate office systems communicate in real-time through networks to satisfy targeted economic, environmental, and safety performance objectives [62]. As a result, the developed conductivity model, modified for continuous flow is valid for MPC and EMPC, and promising for real-time decision-making over the network for better management, energy savings, and handling of market/demand changes in WTPs/WWTPs.

4. Conclusions

WTP/WWTPs have been well-known for their large amounts of data generated with low efficiency of data utilization, operational uncertainty, and fluctuations in water quality/quantity [18,19]. These fluctuations require frequent parameter adjustment and model recalibration during operation for effective MPC, but traditional physics-based mechanistic models are incapable of adapting to these changes in a timely manner [63]. The non-ideal heterogeneous mixing models proposed in this study are simple with few fitting parameters and take much less time for simulation than traditional CFD models. The collected high-resolution sensor data can be instantly transmitted to the model calibration process, ensuring the calibration of non-ideal heterogeneous mixing models in a real-time *in situ* mode during on-going operation.

This unique feature mitigates the severe time-delay problems of traditional pure physics-based models and enables a prompt modification for higher accuracy system identification based on authentic representations of the system. Exploiting this technology within closed-loop control, such as MPC, enables a novel precise control system for WTP/WWTPs.

Moreover, the heterogeneity profiling models can be applied for pattern recognition so as to better understand the internal mechanisms of complex processes (e.g., transport mechanisms of different ions), with or without involving algorithms and redundant equation deduction. Such generalized methodology can serve as a platform for simulating state variables for other chemical species with similar physical principles.

Declaration of Competing Interest

The authors declare that they have no known competing financial interests or personal relationships that could have appeared to influence the work reported in this paper.

Acknowledgments

This study was supported by the National Science Foundation (NSF) Environmental Engineering Program GOALI Project (Grant No.: 1706343), NSF Partnerships for Innovation (PFI) Accelerate Innovative Research (AIR) Project (Grant No: 1640701), NSF I-Corps Project (Grant No: 1655451), and NSF Smart and Connected Communities (SCC) Project (Grant No: ECCS- 2018492), and Connecticut SPARK Program. Any opinions, findings, and conclusions or recommendations expressed in this material are those of the authors and do not necessarily reflect the views of the National Science Foundation.

Appendix A. Supplementary data

Supplementary data to this article can be found online at <https://doi.org/10.1016/j.cej.2021.132819>.

References

- [1] K.V. Gernaey, M.C.M. van Loosdrecht, M. Henze, M. Lind, S.B. Jørgensen, Activated sludge wastewater treatment plant modelling and simulation: state of the art, *Environ. Modell. Software* 19 (9) (2004) 763–783, <https://doi.org/10.1016/j.envsoft.2003.03.005>.
- [2] S.R. Qasim *Wastewater treatment plants: planning, design, and operation* second ed. 1999 Routledge Boca Raton.

- [3] M. Benosman, Model-based vs data-driven adaptive control: An overview, *Int. J. Adapt Control Signal Process.* 32 (5) (2018) 753–776, <https://doi.org/10.1002/acs.v32.510.1002/acs.2862>.
- [4] E. Aydin, Y. Arkun, G. Is, M. Mutlu, M. Dikbas, Plant-wide optimization and control of an industrial diesel hydro-processing plant, *Comput. Chem. Eng.* 87 (2016) 234–245, <https://doi.org/10.1016/j.compchemeng.2016.01.016>.
- [5] I. Takács, G.G. Patry, D. Nolasco, A dynamic model of the clarification-thickening process, *Water Res.* 25 (10) (1991) 1263–1271, [https://doi.org/10.1016/0043-1354\(91\)90066-Y](https://doi.org/10.1016/0043-1354(91)90066-Y).
- [6] P. Roeleveld, M. Van Loosdrecht, Experience with guidelines for wastewater characterisation in the Netherlands, *Water Sci. Technol.* 45 (6) (2002) 77–87, <https://doi.org/10.2166/wst.2002.0095>.
- [7] M. Nasr, in: *Phytobiont and Ecosystem Restitution*, Springer Singapore, Singapore, 2018, pp. 143–160, https://doi.org/10.1007/978-981-13-1187-1_7.
- [8] N. Banadda, I. Nhapi, R. Kimwaga, A review of modeling approaches in activated sludge systems, *Afr. J. Environ. Sci. Technol.* 5 (6) (2011) 397–408, <https://doi.org/10.4314/AJEST.V5I6.71956>.
- [9] S.G. Zimmermann, M. Wittenwiler, J. Hollender, M. Krauss, C. Ort, H. Siegrist, U. von Gunten, Kinetic assessment and modeling of an ozonation step for full-scale municipal wastewater treatment: micropollutant oxidation, by-product formation and disinfection, *Water Res.* 45 (2) (2011) 605–617.
- [10] L. Corominas, X. Flores-Alsina, L. Snip, P.A. Vanrolleghem, Comparison of different modeling approaches to better evaluate greenhouse gas emissions from whole wastewater treatment plants, *Biotechnol. Bioeng.* 109 (11) (2012) 2854–2863, <https://doi.org/10.1002/bit.v109.1110.1002/bit.24544>.
- [11] O. Bernard, Z. Hadj-Sadok, D. Dochain, A. Genovesi, J.-P. Steyer, Dynamical model development and parameter identification for an anaerobic wastewater treatment process, *Biotechnol. Bioeng.* 75 (4) (2001) 424–438, [https://doi.org/10.1002/\(ISSN\)1097-029010.1002/bit.v75.410.1002/bit.10036](https://doi.org/10.1002/(ISSN)1097-029010.1002/bit.v75.410.1002/bit.10036).
- [12] N. Bertola, L. Palladino, A. Bevilacqua, N. Zaritzky, Optimisation of the design parameters in an activated sludge system for the wastewater treatment of a potato processing plant, *J. Food Eng.* 40 (1–2) (1999) 27–33, [https://doi.org/10.1016/S0260-8774\(99\)00034-5](https://doi.org/10.1016/S0260-8774(99)00034-5).
- [13] D. Wang, J. Liu, R. Srinivasan, Data-driven soft sensor approach for quality prediction in a refining process, *IEEE Trans. Ind. Inf.* 6 (1) (2010) 11–17, <https://doi.org/10.1109/TII.2009.2025124>.
- [14] N. Wahab, R. Katebi, J. Balderud, M. Rahmat, Data-driven adaptive model-based predictive control with application in wastewater systems, *IET Control Theory Appl.* 5 (6) (2011) 803–812, <https://doi.org/10.1049/iet-cta.2010.0068>.
- [15] A. Fenu, G. Guglielmi, J. Jimenez, M. Sperandio, D. Saroj, B. Lesjean, C. Brepols, C. Thoeye, I. Nopens, Activated sludge model (ASM) based modelling of membrane bioreactor (MBR) processes: a critical review with special regard to MBR specificities, *Water Res.* 44 (15) (2010) 4272–4294, <https://doi.org/10.1016/j.watres.2010.06.007>.
- [16] C. Rosén, J. Lennox, Multivariate and multiscale monitoring of wastewater treatment operation, *Water Res.* 35 (14) (2001) 3402–3410, [https://doi.org/10.1016/S0043-1354\(01\)00069-0](https://doi.org/10.1016/S0043-1354(01)00069-0).
- [17] L. Belanche, J.J. Valdés, J. Comas, I. Roda, M. Poch, Prediction of the bulking phenomenon in wastewater treatment plants, *Artif. Intell. Eng.* 14 (4) (2000) 307–317, [https://doi.org/10.1016/S0954-1810\(00\)00012-1](https://doi.org/10.1016/S0954-1810(00)00012-1).
- [18] X. Wei, A. Kusiak, Short-term prediction of influent flow in wastewater treatment plant, *Stoch. Env. Res. Risk Assess.* 29 (1) (2015) 241–249, <https://doi.org/10.1007/s00477-014-0889-0>.
- [19] B. Bidar, J. Sadeghi, F. Shahraiki, M.M. Khalilipour, Data-driven soft sensor approach for online quality prediction using state dependent parameter models, *Chemometrics and Intelligent Laboratory Systems* 162 (2017) 130–141, <https://doi.org/10.1016/j.chemolab.2017.01.004>.
- [20] E. Levlin, Conductivity measurements for controlling municipal waste-water treatment, in: J. Lafferty, C. Williams, J. Sahwe-Taylor, R. Zemel, A. Culotta (Eds.), *Advanced in Neural Information Processing Systems 23 (NIPS 2010)*, Vancouver, 2010, pp. 51–62.
- [21] A.W.P.C. SYSTEMS, Why pH Is Important in Wastewater Treatment, 2018. <https://www.alarcop.com/blog/2016/08/02/ph-important-wastewater-treatment/>. (Accessed 10.02 2018).
- [22] S. Ahsan, M.A. Rahman, S. Kaneco, H. Katsumata, T. Suzuki, K. Ohta, Effect of temperature on wastewater treatment with natural and waste materials, *Clean Technol. Environ. Policy* 7 (3) (2005) 198–202, <https://doi.org/10.1007/s10098-005-0271-5>.
- [23] J.E. Falk, R.M. Soland, An algorithm for separable nonconvex programming problems, *Manage. Sci.* 15 (9) (1969) 550–569.
- [24] R. Horst H. Tuy Global optimization: Deterministic approaches third ed. 1996 Springer-Verlag Berlin Heidelberg, Berlin, Germany.
- [25] I. Papamichail, C.S. Adjiman, A rigorous global optimization algorithm for problems with ordinary differential equations, *J. Global Optim.* 24 (1) (2002) 1–33, <https://doi.org/10.1023/A:1016259507911>.
- [26] C.S. Adjiman, C.A. Floudas, Rigorous convex underestimators for general twice-differentiable problems, *J. Global Optim.* 9 (1) (1996) 23–40, <https://doi.org/10.1007/BF00121749>.
- [27] A.B. Singer, *Global dynamic optimization*, Massachusetts Institute Technol. (2004).
- [28] N. Andrei, Interior Point Filter Line Search: IPOPT, in: *Continuous Nonlinear Optimization for Engineering Applications in GAMS Technology*, Springer, Basel, Switzerland, 2017, pp. 415–435.
- [29] A. Waechter, C. Laird, F. Margot, Y. Kawajiri, Introduction to IPOPT: A tutorial for downloading, installing, and using IPOPT, 2009. <https://projects.coin-or.org/Ipopt/browser/stable/3.10/Ipopt/doc/documentation.pdf?format=raw>.
- [30] Z. Xu, W. Zhou, Q. Dong, Y. Li, D. Cai, Y. Lei, A. Bagtzoglou, B. Li, Flat flexible thin milli-electrode array for real-time in situ water quality monitoring in distribution systems, *Environ. Sci. Water Res. Technol.* 3 (5) (2017) 865–874, <https://doi.org/10.1039/C7EW00103G>.
- [31] Z. Xu, Q. Dong, B. Otieno, Y. Liu, I. Williams, D. Cai, Y. Li, Y. Lei, B. Li, Real-time in situ sensing of multiple water quality related parameters using micro-electrode array (MEA) fabricated by inkjet-printing technology (IPT), *Sens. Actuators, B* 237 (2016) 1108–1119, <https://doi.org/10.1016/j.snb.2016.09.040>.
- [32] H.S. Fogler, *Elements of Chemical Reaction Engineering*, fourth ed., Prentice Hall Professional, Hoboken, NJ, 2006.
- [33] R.B. Bird, Transport phenomena, *Appl. Mech. Rev.* 55 (1) (2002) R1–R4, <https://doi.org/10.1115/1.1424298>.
- [34] M.E. Tuckerman, D. Marx, M. Parrinello, The nature and transport mechanism of hydrated hydroxide ions in aqueous solution, *Nature* 417 (6892) (2002) 925–929, <https://doi.org/10.1038/nature00797>.
- [35] P.W. Atkins, J. De Paula, *Physical Chemistry*, second ed., Oxford University Press, New York, NY, 1998.
- [36] M. Tuckerman, K. Laasonen, M. Sprik, M. Parrinello, Ab initio molecular dynamics simulation of the solvation and transport of hydronium and hydroxyl ions in water, *J. Chem. Phys.* 103 (1) (1995) 150–161, <https://doi.org/10.1063/1.469654>.
- [37] R.B. Bird, W.E. Stewart, E.N. Lightfoot, *Transport Phenomena*, second ed., John Wiley & Sons, New York, 2007.
- [38] A.B. Singer, P.I. Barton, Global optimization with nonlinear ordinary differential equations, *J. Global Optim.* 34 (2) (2006) 159–190, <https://doi.org/10.1007/s10898-005-7074-4>.
- [39] J.K. Scott, B. Chachuat, P.I. Barton, Nonlinear convex and concave relaxations for the solutions of parametric ODEs, *Optimal Control Applications and Methods* 34 (2) (2013) 145–163, <https://doi.org/10.1002/oca.v34.210.1002/oca.2014>.
- [40] M.E. Wilhelm, A.V. Le, M.D. Stuber, Global optimization of stiff dynamical systems, *AIChE J.* 65 (12) (2019), e16836, <https://doi.org/10.1002/aic.16836>.
- [41] A.M. Sahlodin, B. Chachuat, Discretize-then-relax approach for state relaxations in global dynamic optimization, *Comput. Aided Chem. Eng.* 28 (2010) 427–432, [https://doi.org/10.1016/S1570-7946\(10\)28072-0](https://doi.org/10.1016/S1570-7946(10)28072-0).
- [42] R. Misener, C.A. Floudas, ANTIGONE: algorithms for continuous/integer global optimization of nonlinear equations, *J. Global Optim.* 59 (2014) 503–526.
- [43] GAMS Development Corporation, *General Algebraic Modeling System (GAMS)*, rel. 24.2.1, GAMS Development Corporation Washington, DC, 2013.
- [44] J. Bezanson, A. Edelman, S. Karpinski, V.B. Shah, Julia: A fresh approach to numerical computing, *SIAM Rev.* 59 (1) (2017) 65–98, <https://doi.org/10.1137/141000671>.
- [45] I. Dunning, J. Huchette, M. Lubin, JuMP: A modeling language for mathematical optimization, *SIAM Rev.* 59 (2017) 295–320.
- [46] M. Gavrilescu, M. Macoveanu, Process engineering in biological aerobic wastewater treatment, *Acta Biotechnol.* 19 (2) (1999) 111–145, [https://doi.org/10.1002/\(ISSN\)1521-384610.1002/abio.v19.210.1002/abio.370190205](https://doi.org/10.1002/(ISSN)1521-384610.1002/abio.v19.210.1002/abio.370190205).
- [47] S. Judd, *The MBR book: principles and applications of membrane bioreactors for water and wastewater treatment*, second ed., Elsevier, Oxford, United Kingdom, 2010.
- [48] APHA, *Standard Methods for the Examination of Water and Wastewater* (18th ed.), American Public Health Association (1992). <https://archive.epa.gov/water/arch/ive/web/html/vms52.html>.
- [49] M. Henze, M.C. van Loosdrecht, G.A. Ekama, D. Brdjanovic, *Biological Wastewater Treatment*, first ed., IWA Publishing, London, 2008.
- [50] O. Bello, Y. Hamam, K. Djouani, Coagulation process control in water treatment plants using multiple model predictive control, *Alexandria Eng. J.* 53 (4) (2014) 939–948, <https://doi.org/10.1016/j.aej.2014.08.002>.
- [51] W. Shen, X. Chen, M. Pons, J. Corriou, Model predictive control for wastewater treatment process with feedforward compensation, *Chem. Eng. J.* 155 (1–2) (2009) 161–174, <https://doi.org/10.1016/j.cej.2009.07.039>.
- [52] B. Holanda, E. Domokos, A. Reedy, J. Fazakas, Dissolved oxygen control of the activated sludge wastewater treatment process using model predictive control, *Comput. Chem. Eng.* 32 (6) (2008) 1270–1278, <https://doi.org/10.1016/j.compchemeng.2007.06.008>.
- [53] B.W. Bequette, *Process Control: Modeling, Design, and Simulation*, first ed., Prentice Hall Professional, Troy, NY, 2003.
- [54] M. Ellis, H. Durand, P.D. Christofides, A tutorial review of economic model predictive control methods, *J. Process Control* 24 (8) (2014) 1156–1178, <https://doi.org/10.1016/j.jprocont.2014.03.010>.
- [55] J. Zeng, J. Liu, Economic model predictive control of wastewater treatment processes, *Ind. Eng. Chem. Res.* 54 (21) (2015) 5710–5721, <https://doi.org/10.1021/ie504995n>.
- [56] S. Revollar, P. Vega, M. Francisco, R. Vilanova, I. Santín, in: *Optimization of economic and environmental objectives in a Non Linear Model Predictive Control applied to a wastewater treatment plant*, IEEE, Sinaia, Romania, 2016, pp. 318–323.
- [57] R. Horst, H. Tuy, *Global optimization: deterministic approaches*, Springer Science & Business Media, New York, NY, 2013.
- [58] J. Bateman, C. Stevens, W. Mercer, E. Carstensen, Relative humidity and the killing of bacteria: the variation of cellular water content with external relative humidity or osmolality, *Microbiology* 29 (2) (1962) 207–219, <https://doi.org/10.1099/00221287-29-2-207>.
- [59] E. Levlin, Conductivity measurements for controlling municipal waste-water treatment, *Proceedings of a Polish-Swedish-Ukrainian Seminar*, Utron, 2010.
- [60] C. Geankoplis, *Transport Processes and Separation Process Principle (includes unit operations)*, fourth ed., United States, Upper Saddle River, NJ, Prentice-Hall International, 2003.

- [61] D.A. Tillman, D.N.B. Duong, N.S. Harding, Chapter 7 - Modeling and Fuel Blending, in: D.A. Tillman, D.N.B. Duong, N.S. Harding (Eds.), *Solid Fuel Blending*, Butterworth-Heinemann, Boston, 2012, pp. 271–293.
- [62] P.D. Christofides, J.F. Davis, N.H. El-Farra, D. Clark, K.R.D. Harris, J.N. Gipson, Smart plant operations: Vision, progress and challenges, *AIChE J.* 53 (11) (2007) 2734–2741, [https://doi.org/10.1002/\(ISSN\)1547-590510.1002/aic.v53:1110.1002/aic.11320](https://doi.org/10.1002/(ISSN)1547-590510.1002/aic.v53:1110.1002/aic.11320).
- [63] J.-P. Ylén, Measuring, modelling and controlling the pH value and the dynamic chemical state, Helsinki University of Technology, 2001.
- [64] Z. Xu, F. MahmoodPoor Dehkordy, Y. Li, Y. Fan, T. Wang, Y. Huang, W. Zhou, Q. Dong, Y.u. Lei, M.D. Stuber, A. Bagtzoglou, B. Li, High-fidelity profiling and modeling of heterogeneity in wastewater systems using milli-electrode array (MEA): Toward high-efficiency and energy-saving operation, *Water Res.* 165 (2019) 114971, <https://doi.org/10.1016/j.watres.2019.114971>.
- [65] M.E. Wilhelm, M.D. Stuber, EAGO.jl: Easy advanced global optimization in Julia, *Optimization Methods & Software* (2020), <https://doi.org/10.1080/10556788.2020.1786566>.
- [66] M. Schmidt, H. Lipson, Distilling free-form natural laws from experimental data, *Science* 324 (5923) (2009) 81–85, <https://doi.org/10.1126/science.1165893>.

Supplementary Information

Precise control of water and wastewater treatment systems with non-ideal heterogeneous mixing models and high-fidelity sensing

Tianbao Wang ^a, Chenyu Wang ^b, Zhiheng Xu ^a, Can Cui ^c, Xingyu Wang ^a, Zoe Demitrack ^a, Zheqin Dai ^a, Amvrossios Bagtzoglou ^a, Matthew D. Stuber ^{*b}, Baikun Li^{*a}

^a Department of Civil & Environmental Engineering, University of Connecticut, Storrs, Connecticut 06269, United States

^b Department of Chemical and Biomolecular Engineering, University of Connecticut, Storrs, Connecticut 06269, United States

^c Department of Material Science and Engineering, University of Connecticut, Storrs, Connecticut 06269, United States

Tianbao Wang and Chenyu Wang share co-first authorship.

*Corresponding authors: stuber@alum.mit.edu, baikun.li@uconn.edu

S1. Development of pH Mixing Models

The development of pH mixing models for three independent studies with shock injection in the high, middle, and low zone are introduced in this section. The high zone injection model is introduced in Section 2.2.2 in the main manuscript, established as:

$$\begin{aligned}\frac{dH_1}{dt} &= \frac{1}{v_1V} (H_0 + \kappa_1 H_4 - \kappa_1 H_1), \\ \frac{dH_2}{dt} &= \frac{1}{v_2V} (\kappa_1 H_1 + \kappa_2 H_4 - (\kappa_1 + \kappa_2) H_2), \\ \frac{dH_3}{dt} &= \frac{1}{v_3V} ((\kappa_1 + \kappa_2) H_2 + \kappa_3 H_4 - (\kappa_1 + \kappa_2 + \kappa_3) H_3), \\ \frac{dH_4}{dt} &= \frac{1}{(1 - v_1 - v_2 - v_3)V} ((\kappa_1 + \kappa_2 + \kappa_3) H_3 - (\kappa_1 + \kappa_2 + \kappa_3) H_4).\end{aligned}\tag{S1}$$

In this model, H_i represents the pH corresponding to each zone ($i=1,2,3,4$) in the reactor, v is the volume fraction of different zones, and κ is the superficial transport coefficient indicating the “flow rate” of OH^- between adjacent zones that accounts for both reaction and convection transport (L/s). As illustrated in Fig. 2d of the main manuscript, the flow rates were set as: $f_{4,1} = \kappa_1$, $f_{4,2} = \kappa_2$, $f_{4,3} = \kappa_3$, $f_{1,2} = \kappa_1$, $f_{2,3} = \kappa_1 + \kappa_2$, $f_{3,4} = \kappa_1 + \kappa_2 + \kappa_3$ based on the principle of mass conservation (assuming constant density). H_0 represents the input of the shock KOH which is equal to H_v during the injection period (0-8s) defined as:

$$H_0 = \begin{cases} H_v, & 0 < t < 8 \\ 0, & 8 < t < 200 \end{cases}\tag{S2}$$

In this model, the parameters κ_1 , κ_2 , κ_3 and H_v in addition to the volume fractions v_1 , v_2 and v_3 are considered to be uncertain parameters requiring estimation by deterministic global optimization.

As for the case of KOH shock injection in the middle zone (Fig. 2e of the main manuscript), the model was established as:

$$\begin{aligned}\frac{dH_1}{dt} &= \frac{1}{v_1 V} (\kappa_1 H_2 - \kappa_1 H_1), \\ \frac{dH_2}{dt} &= \frac{1}{v_2 V} (H_0 + (\kappa_1 + \kappa_2) H_4 - (\kappa_1 + \kappa_2) H_2), \\ \frac{dH_3}{dt} &= \frac{1}{v_3 V} (\kappa_2 H_2 + \kappa_3 H_4 - (\kappa_2 + \kappa_3) H_3), \\ \frac{dH_4}{dt} &= \frac{1}{(1 - v_1 - v_2 - v_3) V} (\kappa_1 H_1 + (\kappa_2 + \kappa_3) H_3 - (\kappa_1 + \kappa_2 + \kappa_3) H_4).\end{aligned}\tag{S3}$$

In this model, the corresponding flow rates were defined as: $f_{2,1} = \kappa_1$, $f_{2,3} = \kappa_2$, $f_{4,3} = \kappa_3$, $f_{1,4} = \kappa_1$, $f_{4,2} = \kappa_1 + \kappa_2$, and $f_{3,4} = \kappa_1 + \kappa_2 + \kappa_3$. The initial injection shock of KOH also followed the previous principle (S2). The volumes of the pH sensor zones were assumed to remain the same fraction values based on the injection position, which can be confirmed from the global optimization results of the high zone injection case. Thus, the volume fractions were not estimated in this model. The superficial transport coefficients κ_1 , κ_2 , κ_3 and the input H_v were considered as uncertain parameters in the system requiring to be determined by global optimization.

The model corresponding to the KOH shock injection in the low zone (Fig. 2f of the main manuscript) was established as:

$$\frac{dH_1}{dt} = \frac{1}{v_1 V} ((\kappa_1 + \kappa_2)H_2 - (\kappa_1 + \kappa_2)H_1), \quad (\text{S4})$$

$$\frac{dH_2}{dt} = \frac{1}{v_2 V} (\kappa_1 H_3 + \kappa_2 H_4 - (\kappa_1 + \kappa_2)H_2),$$

$$\frac{dH_3}{dt} = \frac{1}{v_3 V} (H_0 + (\kappa_1 + \kappa_3)H_4 - (\kappa_1 + \kappa_3)H_3),$$

$$\frac{dH_4}{dt} = \frac{1}{(1 - v_1 - v_2 - v_3)V} ((\kappa_1 + \kappa_2)H_1 + \kappa_3 H_3 - (\kappa_1 + \kappa_2 + \kappa_3)H_4).$$

Here, based on the conservation law, the flow rates are set as: $f_{3,2} = \kappa_1$, $f_{4,2} = \kappa_2$, $f_{3,4} = \kappa_3$, $f_{2,1} = \kappa_1 + \kappa_2$, $f_{1,4} = \kappa_1 + \kappa_2$, and $f_{4,3} = \kappa_1 + \kappa_3$. Similarly, the volume fractions of the sensor zones were obtained by the high zone injection optimization results. Furthermore, the global optimization problem was formulated to verify the superficial transport coefficient κ_1 , κ_2 , κ_3 and the shock H_v .

S2. Global Optimization Formulation and Validation for Temperature Mixing Model

Based on the energy balance for the batch system, a single equation is used to model the bulk fluid temperature:

$$\frac{dT}{dt} = -\frac{UA_c}{V\rho C_p}(T - T_c). \quad (\text{S5})$$

Here, T is the temperature of the water solution ($^{\circ}\text{C}$) and A_c is the cross-sectional area of the cylindrical container (m^2) across which heat transfer is occurring. The height of the container can be derived as: $L = V/A_c = 0.16\text{m}$. ρ and C_p are respectively the density (kg/m^3) and heat capacity ($\text{kJ}/(\text{kg}\cdot^{\circ}\text{C})$) of the water ($\rho = 998.19$, $C_p = 4.18$). T_c is the temperature of the inner face of the bottom of the reactor and U is the overall heat transfer coefficient of the system ($\text{kW}/(\text{m}^2\cdot^{\circ}\text{C})$). In this model, the inner wall on the bottom of the reactor is considered as the heated surface for convective heat transfer. Thus, U is simplified to the convective heat transfer coefficient for the liquid in the tank h_l . The initial condition of this system was set as $T(t = 0) = T_0 = 18.5^{\circ}\text{C}$.

The temperature mixing model (S5) can be directly solved analytically to obtain the explicit closed-form solution as:

$$T = T_c + (T_0 - T_c) \exp\left[-\frac{Ut}{L\rho C_p}\right]. \quad (\text{S6})$$

Therefore, the global optimization problem for the heat transfer model can be easily solved by directly using the analytical solution (S6):

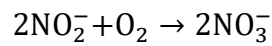
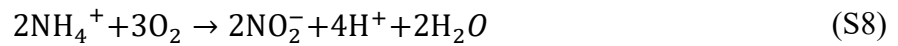
$$\begin{aligned} & \min_{T_i \in \mathcal{T} \subset \mathbb{R}, \mathbf{p} \in \Pi \subset \mathbb{R}^{np}} \sum_{i=1}^N \sum_{j=1}^3 (T_i - T_{i,j}^{data}) \\ \text{s.t. } & T_i = T_c + (T_0 - T_c) \exp\left[-\frac{Ut_i}{h\rho C_p}\right], \quad i = 1, \dots, N \end{aligned} \quad (\text{S7})$$

The objective function was defined as the SSE between the temperature calculated from the model and the data in different sensor zones. The unknown parameters are the heat transfer coefficient $U \in [0.5, 5.0]$ and the temperature of the heated surface $T_c \in [20, 200]$.

S3. Development of A Continuous Flow Conductivity Transport Model for Nitrification

CSTR

In this section, details on the case study of wastewater treatment simulations in a continuous flow nitrification reactor (Figure 2c of the main manuscript) are introduced. The CSTR volume is set as 1000 L. Based on the standard of moderate municipal wastewater [1], the operating setpoint is set at 280 $\mu\text{S}/\text{cm}$ corresponding to the standard concentration. To meet this specification, biological nitrification processes are applied to oxidize ammonia in wastewater [2]. In this tank reactor, a continuous atmospheric air stream is supplied at the bottom for removing excess ammonia through the following two-step nitrification process:



First, ammonium ions are oxidized to nitrite ions in the nitrification step and then the nitrite ions are further oxidized to nitrate ions in the nitrification step. In practice, the first step is carried out by the ammonia oxidizing bacteria (AOB) and the second step is carried out by the nitrite oxidizing bacteria (NOB) [2]. In general, 4.5 mg of oxygen is required to fully nitrify 1 mg of N-NH_4^+ . Molecular biology studies indicate that AOB predominates the nitrification process [3]. Thus, a simplified kinetic model for oxygen consumption is considered in this paper. It is assumed that there are volatile suspended solids (VSS) in the system that are necessary for nitrification and the initial biomass concentration was in the range of 1.4 to 1.6 g-VSS/L. The ammonium consumption rate $r_{\text{NH}_4^+}$ counted as nitrogen (mg N-NH_4^+ /(L·min)) in the reaction is given by:

$$r_{\text{NH}_4^+} = -r_{\text{AOB}}X_{\text{AOB}}, \quad (\text{S9})$$

where X_{AOB} is the concentration of AOB (mg VSS/L), and r_{AOB} is the ammonium oxidation rate (mg N-NH_4^+ /(g VSS·min)) that is given by:

$$r_{AOB} = r_{AOB,max} \frac{c_{NH_4^+}}{K_{SAOB} + c_{NH_4^+} + \frac{c_{NH_4^+}^2}{K_{IAOB}}} \frac{c_O}{K_{OAOB} + c_O} \quad (S10)$$

In this formula, $r_{AOB,max}$ is the maximum nitrification rate (mg N-NH₄⁺/(g VSS·min)), K_{SAOB} is the Monod constant of ammonia for AOB (mg N-NH₄⁺/L), K_{IAOB} is the inhibition constant of ammonia for AOB ((mg N-NH₄⁺/L), c_O is the dissolved oxygen concentration (mg/L), and K_{OAOB} is the Monod constant of oxygen for AOB (mg/L). In this project, it is assumed that oxygen is growth limiting since ammonium is always in excess (around 30 mg N-NH₄⁺/L) and the corresponding attributing coefficient is $c_{NH_4^+} / (K_{SAOB} + c_{NH_4^+} + c_{NH_4^+}^2 / K_{IAOB}) \approx 1$. Thus, the ammonium oxidation rate (S10) can be simplified to $r_{AOB} = r_{AOB,max} c_O / (K_{OAOB} + c_O)$, which is only related to oxygen concentration.

The oxygen balance for the nitrification reaction is given by:

$$\frac{dc_O}{dt} = -r_{AOB} \psi_{AOB} X_{AOB} + k_{la} \cdot (c_O^* - c_O), \quad (S11)$$

where ψ_{AOB} is the stoichiometric ratio between oxygen and ammonia (mg O₂/mg N-NH₄⁺), the term $k_{la} \cdot (c_O^* - c_O)$ represents the rate of mass transfer of oxygen into the liquid from air bubbles, k_{la} is the volumetric mass transfer coefficient (s⁻¹) [4], and c_O^* is the saturated dissolved oxygen concentration (9.1 mg/L at 20 °C) [5]. The standard oxygen transfer rate (SOTR, mg/s) is defined as $SOTR = k_{la} \cdot c_O^* \cdot V$ that represents the amount of oxygen transferred per second at 20 °C. The standard oxygen transfer efficiency (SOTE, %) refers to the ratio of oxygen in inlet air stream dissolved in liquid at 20 °C that is given by $SOTE = SOTR / W_O$, with W_O the mass flow of oxygen in the air stream (mg/s). W_O can be calculated by an empirical formula: $W_O = 0.2967Q$, where Q is the airflow rate at 20 °C. Therefore, the oxygen transfer rate (S11) can be rewritten as:

$$\frac{dc_o}{dt} = -r_{\text{AOB}}\psi_{\text{AOB}}X_{\text{AOB}} + \frac{0.2967Q \cdot \text{SOTE}}{V} \left(1 - \frac{c_o}{c_o^*}\right). \quad (\text{S12})$$

All the relevant parameter values are summarized in [Table S6](#).

The modified conductivity mixing model is introduced in **Section 3.4**:

$$\frac{dC_i}{dt} = \frac{1}{4V} (k_i(C_4 - C_i) + \dot{m}_{\text{in},i}C_{\text{in},i} - \dot{m}_{\text{out}}C_i) + R_{\text{NH}_4^+}, \quad i = 1,2,3 \quad (\text{S13})$$

$$\frac{dC_4}{dt} = \frac{1}{4V} k_4(C_1 + C_2 + C_3 - 3C_4) + R_{\text{NH}_4^+},$$

where $\dot{m}_{\text{in},i}$ and $\dot{m}_{\text{out},i}$ are continuous inlet and outlet flow rate at zone i (L/s), respectively, $C_{\text{in},i}$ represents the conductivity of the inlet stream at zone i ($\mu\text{S}/\text{cm}$), and $R_{\text{NH}_4^+}$ is the reaction rate law for NH_4^+ consumption counted as conductivity ($\mu\text{S}/\text{cm}/\text{s}$). When substituting the reaction rate $r_{\text{NH}_4^+}$ (S9) to the modified model (S13), the ammonium concentration should be converted to conductivity for consistency. The converting relationship is linear and can be directly derived as $C_{\text{NH}_4\text{Cl}} = 10.78 + 1.323\text{E}5c_{\text{NH}_4\text{Cl}}$ by linear regression of the data from CRC handbook listed in [Table S4](#) [3, 6]. Ideally, the mass transfer coefficients k_1 , k_2 , k_3 and k_4 should be able to account for all situations with inlet conductivity shocks at high, middle or low zones since in a real system we would not have *a priori* knowledge of the heterogeneity before measurement. However, as we can see from the previous optimization results, the shock experiments resulted in slightly differing values for these coefficients as indicated in [Table S3\(a\)](#). Thus, the mass transfer coefficients were taken as the average of the optimal mass transfer coefficients from the original conductivity transport models for high injection and middle injection cases. The low zone injection case was excluded here as its corresponding optimal value for k_2 differed dramatically from the optimal values for the other cases; most likely due to the very close proximity to the adjacent mixing zone. Then the mass transfer coefficients were scaled based on the nitrification CSTR volume. We

conduct simulations by substituting the average mass transfer coefficients and verify that as a whole, the simulated profiles conformed to the original experimental data (even for the low zone injection case, the simulated profile can be adjusted to coincide with the experimental profile by using the average C_v from high zone and middle zone injection cases to replace C_v from low zone injection case). The mass transfer coefficients of this continuous flow conductivity model are listed in [Table S6](#). The modified continuous flow conductivity model (S13) combined with the oxygen transfer model (S12) can be deemed as a new system of ODEs for simulating a segment of a continuous biological nutrient removal step with heterogeneous mixing. The explicit Euler method is employed for integrating the combined system of ODEs to simulate the conductivity profiles in each zone.

A proportional-integral (PI) controller was designed to control the aeration for high-zone influent conductivity shock rejection. The overall control law is defined as:

$$u(t) = K_p e(t) - K_i \int_0^t e(t') dt'$$

where $u(t)$ is the control variable that is equal to the aeration airflow rate Q (mg/s) in this study. $e(t) = SP - C_1(t)$ is the error value as the difference between the desired setpoint (SP) and a measured process variable, which is the high-zone conductivity in this study $C_1(t)$. K_p and K_i are the coefficients for the proportional and integral terms, respectively. These two coefficients are obtained by fitting dynamic input and output data to a first-order plus dead-time model and then tuned. First, the Internal Model Control (IMC) rules are used for tuning. Then the parameters are further adjusted manually until the closed-loop systems perform as desired. The final values of the PI parameters used in this study are $K_p = -74.941$ and $K_i = -0.07419$.

S4. Global Optimization Formulation for Conductivity and pH Mixing Model

For the conductivity and pH models, analytical solutions of the corresponding systems of ordinary differential equations (ODEs) do not exist. Thus, numerical methods must be applied to compute the numerical solutions of the systems of ODEs. The time domain I was discretized into $N = (t_f - t_0)/\Delta t$ time steps and then the explicit Euler algorithm was used for discretizing the ODEs to obtain a discrete-time system. Consequently, the discrete-time dynamic optimization problem was obtained by:

$$\begin{aligned} & \min_{\mathbf{x}_i \in X \subset \mathbb{R}^{n_x}, \mathbf{p} \in \Pi \subset \mathbb{R}^{n_p}} \sum_{\tau=1}^{N_\tau} \sum_{j=1}^3 (x_{\tau,j} - x_{\tau,j}^{data})^2 & (S14) \\ \text{s.t. } & \mathbf{x}_{i+1} = \mathbf{x}_i + h\mathbf{f}(\mathbf{x}_i, \mathbf{p}), \quad i = 0, 1, \dots, N-1 \\ & \mathbf{x}_0 = \mathbf{z}_0 \end{aligned}$$

where the sum-of-squared errors (SSE) as the objective function was sought to minimize between the state variable $x_{\tau,j}$ calculated from the model and the experimental data $x_{\tau,j}^{data}$ at τ time node for all of three sensor zones. Here, the initial condition was taken as a constant value \mathbf{z}_0 , and a representative subset of the raw data was taken to construct the objective function for simplification of the mathematical structure and acceleration of global optimization calculation. Specifically, the index of the data point with the highest measured value was chosen in the dataset at the injection sensor zone (i_{max}). The time period before i_{max} was considered as the ‘‘injection period’’ and the time period after i_{max} is considered as the ‘‘dilution period’’. Five equidistant points (i_{max} not included) in the injection period, 15 equidistant points (i_{max} not included) in the dilution period and i_{max} were selected to compose the selected subset which had $N_\tau = 21$ nodes. The distance between each node was rounded to an integer for ease of obtaining the index set. The equality constraints of these discrete-time dynamic optimization problems are the numerical expressions of the discretized ODE system using explicit Euler over the entire time horizon, which

had $n_p N$ equations in total. As for the conductivity models, the uncertain parameter vector was defined as $\mathbf{p} = (k_1, k_2, k_3, k_4, C_v)$ for high, middle, and low injection zones. The lower bounds and upper bounds of the parameters are listed in [Table S7 \(a\)](#).

To validate the pH model with the experimental data, the global optimization problem was first solved for the high zone pH shock injection. The unknown parameters for this problem were defined as $\mathbf{p} = (v_1, v_2, v_3, \kappa_1, \kappa_2, \kappa_3, H_v)$. The uncertainty intervals for these parameters are listed in [Table S7 \(b\)](#). After solving the problem for high zone injection case to global optimality, the optimal volume fractions were taken and fixed as the volume fractions for the middle and low zone injection as listed in [Table S2](#). Therefore, for the middle zone and low zone parameter estimation problems, we only estimated four parameters $\mathbf{p} = (\kappa_1, \kappa_2, \kappa_3, H_v)$ with uncertainty listed in [Table S7 \(b\)](#).

S5. Calibration Process for Revised Conductivity and pH Mixing Models for Additional Experiments

The calibration process for revised conductivity mixing models for KCl and MgSO₄ experiments is summarized in this section. The critical parameter C_v in the model was adjusted to mitigate mismatch with the experimental data. Since the shock conductivity dilutes immediately after injection, C_v represents the conductivity inside the reactor tank instantly after injection in inverse proportion to injection time. Therefore, C_v was adjusted for the KCl and MgSO₄ experiments to be 4.5 times (36s/8s) and 18 times (36s/2s) that of the original NaCl experiments on the basis of the time to peak for conductivity. Furthermore, an additional modification was required to reconcile the difference between ionic species. Based on the dependence of electrical conductivity on concentration as mass percent (%), as listed in [Table S4](#), the units of shock concentrations for NaCl, KCl, and MgSO₄ (100g/L) were first converted to mass percentage and the corresponding conductivities were calculated by interpolation. Finally, C_v for the KCl and MgSO₄ experiments was further modified by the ratio of conductivity for KCl and MgSO₄ solution to NaCl solution (136.29/120.29 and 40.90/120.29), respectively.

As for calibration for pH mixing model for NaOH experiment, the H_v parameter is inversely proportional to the apparent injection time (8s for original KOH experiment; 1.9s for NaOH experiment). We adjusted the H_v based on the ratio of the apparent injection times for the KOH experiment to the NaOH experiments (8s/1.9s) and re-simulated using the modified H_v .

S6. Development of Computational Fluid Dynamics (CFD) Models

Numerical finite element models were developed in COMSOL Multiphysics (COMSOL, Inc, Burlington, MA, USA). Flow in the reactor was modeled by the Navier-Stokes equations using the Arbitrary Lagrangian-Eulerian (ALE) techniques [6]:

$$\frac{\partial \rho}{\partial t} - \frac{\partial x}{\partial t} \cdot \nabla \rho + \nabla \cdot (\rho u) = 0$$

$$\rho \left(\frac{\partial u}{\partial t} - \frac{\partial x}{\partial t} \cdot \nabla u \right) + \rho (u \cdot \nabla) u = \nabla \cdot [-pI + \tau] + F$$

Here, ρ is density, $u = v + \frac{\partial r}{\partial t}$, where v is the velocity vector in the rotating coordinate system, and r is the position vector, t is the mesh reference time, x is a function of angular velocity and time, p is pressure, τ is shear stress, and F is the external force vector. To simulate the flow in the reactor, a fixed domain and a rotating domain were defined and coupled using a continuity boundary condition on the common interior walls [7].

Table S1 Nomenclature

Notation		Subscript	
A	Cross-sectional Area [m^2]	0	Injection
C	Conductivity [$\mu\text{S}/\text{cm}$]	1	High zone
c	Concentration [mg/L]	2	Middle zone
C_{in}	Conductivity in the inlet stream [$\mu\text{S}/\text{cm}$]	3	Low zone
C_p	Heat capacity [$\text{kJ}/(\text{kg} \cdot ^\circ\text{C})$]	4	Mixing zone
D	Discharge [$\mu\text{S}/\text{cm}$]	c	Cross-section of the container
H	Alkalinity pH of a solution	f	End
h	Heat transfer coefficient [$\text{kW}/(\text{m}^2 \cdot ^\circ\text{C})$]	l	Liquid
k	Mass transfer coefficient [L/s]	O	Oxygen
k_{la}	Volumetric mass transfer coefficient [s^{-1}]	s	Solid
L	Height [m]	v	Shock
M	Control horizon	w	Wall
\dot{m}_{in}	Continuous inlet flow rate [L/s]		
\dot{m}_{out}	Continuous outlet flow rate [L/s]		
p	Parameter		
P	Prediction horizon		
Q	Air flow rate [mg/s]		
R	Reaction rate counted as conductivity [$\mu\text{S}/\text{cm}/\text{s}$]		
r	Reaction rate counted as concentration [$\text{mg}/\text{L}/\text{s}$]		
SP	Setpoint [$\mu\text{S}/\text{cm}$]		
SOTE	Standard oxygen transfer efficiency [%]		
SOTR	Standard oxygen transfer rate [mg/s]		
T	Temperature of the solution [$^\circ\text{C}$]		
t	Time [s]		
U	Overall heat transfer coefficient [$\text{kW}/(\text{m}^2 \cdot ^\circ\text{C})$]		
u	Control variable		
V	Container volume [L]		
W	Mass flow rate in air stream [kg/s]		
w	Penalty coefficient		
x	State variable		
ρ	Density [kg/m^3]		
δ	Control action step size [s]		

Table S2 The global optimal parameter values obtained from (a) the conductivity parameter estimation problems, and (b) the optimal parameter values obtained from the pH parameter estimation problems.

Conductivity (a)		k_1^*	k_2^*	k_3^*	k_4^*	C_v^*
High zone injection		2.376E-03	1.411E-03	1.504E-03	0.9477	428.46
Middle zone injection		1.385E-03	2.914E-03	2.577E-03	1.8990	412.37
Low zone injection		2.283E-03	2.9234	7.761E-03	0.5995	182.53

pH (b)		v^*	κ_1^*	κ_2^*	κ_3^*	H_v^*
High zone injection	v_1^*	3.937E-01				
	v_2^*	1.990E-03	1.155E-02	3.464E-03	4.214E-03	0.1413
	v_3^*	5.412E-03				
Middle zone injection	v_1	1.990E-03				
	v_2	3.937E-01	3.012E-02	1.107E-02	2.174E-03	0.1458
	v_3	5.412E-03				
Low zone injection	v_1	1.990E-03				
	v_2	5.412E-03	2.142E-02	8.912E-03	6.346E-03	0.1469
	v_3	3.937E-01				

Table S3 Time cost for solving conductivity and pH global optimization problems for independent high-zone, middle-zone and low-zone injection experiments, are reported in this table.

Time (s)	Conductivity model	pH model
High-zone injection	214.55	483.96
Middle-zone injection	4038.74	9.559
Low-zone injection	372.34	8.922

Table S4 Electrical conductivity (mS/cm) for NaCl, KCl, and MgSO₄ at different mass percentages [8].

Mass percent	0.5%	1%	2%	5%	10%	15%	20%	25%
NaCl	8.2	16.0	30.2	70.1	126	171	204	222
KCl	8.2	15.7	29.5	71.9	143	208	-	-
MgSO₄	4.1	7.6	13.3	27.4	42.7	54.2	51.1	44.1

Table S5 This table contains the data (in percentages) for environmental discharge and energy usage from the no control, open-loop control, PI control, MPC, EMPC1, and EMPC2 simulations.

Percentage		No Control	Open Loop	PI	MPC	EMPC1	EMPC2
High Zone Shock	Discharge	100	22.342	44.055	30.676	26.094	28.097
	Energy	45.818	100	61.137	57.849	63.438	60.317
Middle Zone Shock	Discharge	100	20.482	45.292	29.791	24.486	26.721
	Energy	45.818	100	52.552	56.624	62.476	59.086
Low Zone Shock	Discharge	100	21.254	45.498	30.148	25.165	27.294
	Energy	45.818	100	52.951	57.129	62.469	59.674
Multiple Shocks	Discharge	100	49.673	66.71	52.869	50.525	51.514
	Energy	45.818	100	80.271	70.185	75.507	72.578

Table S6 The parameters for continuous flow conductivity mixing model are summarized in this table.

Name	Symbol	Value	Reference
High zone mass transfer coefficient [L/s]	k_1	4.9478	This Study
Middle zone mass transfer coefficient [L/s]	k_2	5.6907	This Study
Low zone mass transfer coefficient [L/s]	k_3	5.3694	This Study
Mixing zone mass transfer coefficient [L/s]	k_4	3745.6	This Study
CSTR volume [L]	V	1000	This Study
Continuous inlet flow rate [L/s]	\dot{m}_{in}	1.042	This Study
Continuous outlet flow rate [L/s]	\dot{m}_{out}	1.042	This Study
Concentration of AOB [mg VSS/L]	X_{AOB}	505	[3]
Monod constant of ammonia for AOB [mg N-NH ₄ ⁺ /L]	K_{SAOB}	0.24	[9]
Inhibition constant of ammonia for AOB [mg N-NH ₄ ⁺ /L]	K_{IAOB}	6200	[9]
Monod constant of oxygen for AOB [mg/L]	K_{OAOB}	0.3	[9]
Stoichiometric ratio between oxygen and ammonia [mg O ₂ /mg N-NH ₄ ⁺]	Ψ_{OAOB}	2.5	[9]
Saturated dissolved oxygen concentration [mg/L]	c_{O^*}	9.1	[5]
Standard oxygen transfer efficiency [%]	SOTE	10	[10]

Table S7 The lower and upper bounds for uncertain parameters in nonideal heterogeneous mixing models (a: conductivity, b: pH)

Parameters (a)	High injection		Middle injection		Low injection	
	Lower bounds	Upper bounds	Lower bounds	Upper bounds	Lower bounds	Upper bounds
k_1	2.0E-3	2.5E-3	1E-3	5E-3	2.0E-3	2.5E-3
k_2	1.2E-3	1.7E-3	1E-3	5E-3	1.5	3.0
k_3	1.2E-3	1.7E-3	1E-3	5E-3	7.5E-3	8.0E-3
k_4	0.85	0.95	1.0	2.0	0.5	1.0
C_v	420	430	400	450	150	200

Parameters (b)	High injection		Middle injection		Low injection	
	Lower bounds	Upper bounds	Lower bounds	Upper bounds	Lower bounds	Upper bounds
v_1	0.25	0.55				
v_2	1E-3	1E-2				
v_3	1E-3	1E-2				
κ_1	5E-3	1.5E-2	1E-3	1E-1	5E-4	5E-2
κ_2	1E-3	1E-2	1E-3	1E-1	1E-4	1E-2
κ_3	1E-3	1E-2	1E-3	1E-1	1E-4	1E-2
H_v	1E-1	2E-1	1E-1	2E-1	1E-1	2E-1

Table S8 The physical properties of water at 20°C are presented below.

Physical property	Symbol	Value
Density [kg/m ³]	ρ	998.19
Viscosity [Pa·s]	μ	1.002E-3
Heat capacity [kJ/(kg·°C)]	C_p	4.18
Thermal conductivity [W/(m·°C)]	λ	0.5973
Prandtl number	Pr	7.2059

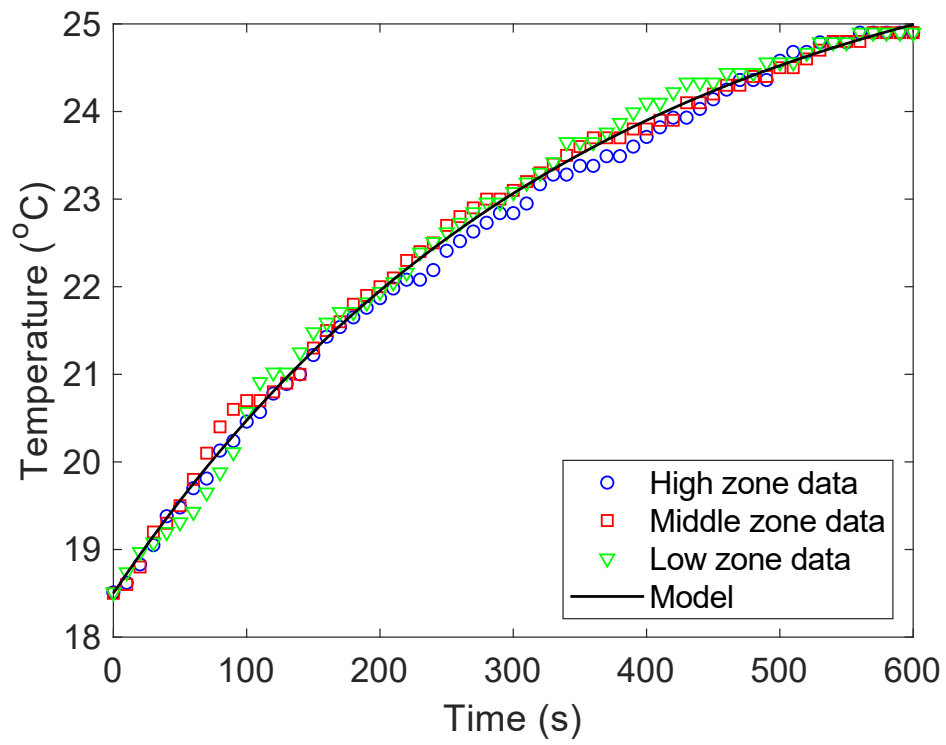


Figure S1 The optimal temperature profile (black solid line) from the global optimization results is plotted versus the measured temperature sensor data in high zone (blue circle), middle zone (red square), and low zone (green triangle).

Primary Options:

Formula building-blocks:	Name	Complexity	Currently Selected:	
Basic				
<input checked="" type="checkbox"/>	Constant	1	c, x, +, -, *, /	
<input type="checkbox"/>	Integer Constant	1		
<input checked="" type="checkbox"/>	Input Variable	1		
<input checked="" type="checkbox"/>	Addition	1		
<input checked="" type="checkbox"/>	Subtraction	1		
<input checked="" type="checkbox"/>	Multiplication	1		
<input checked="" type="checkbox"/>	Division	2		
<input type="checkbox"/>	Negation	1		
Trigonometry				
<input type="checkbox"/>	Sine	3		
<input type="checkbox"/>	Cosine	3		
<input type="checkbox"/>	Tangent	4		
Exponential				
<input type="checkbox"/>	Exponential	4		
<input type="checkbox"/>	Natural Logarithm	4		
<input type="checkbox"/>	Factorial	4		
<input type="checkbox"/>	Power	5		
<input type="checkbox"/>	Square Root	4		
Squashing				
<input type="checkbox"/>	Logistic Function	4		
<input type="checkbox"/>	Step Function	4		
<input type="checkbox"/>	Sign Function	4		
<input type="checkbox"/>	Gaussian Function	4		
<input type="checkbox"/>	Hyperbolic Tangent	4		
<input type="checkbox"/>	Error Function	4		
<input type="checkbox"/>	Complementary Error Function	4		

Error metric: Squared error

Row Weight: <none>

Data Splitting: Treat all data points equally (default)

Figure S2 The options of formula building-blocks were selected as Constant, Input Variable, Addition, Subtraction, Multiplication, Division. The target formula was set as $D(\sigma_{top}, t) = f(\sigma_{top}, \sigma_{middle}, \sigma_{deep})$, where σ_{top} , σ_{middle} , σ_{deep} are the conductivity values from high sensor, middle sensor, and low sensor, respectively.

References

- [1] M. Henze, M.C. van Loosdrecht, G.A. Ekama, D. Brdjanovic, *Biological Wastewater Treatment*, first ed., IWA Publishing, London, 2008.
- [2] S. Siripong, B.E. Rittmann, Diversity study of nitrifying bacteria in full-scale municipal wastewater treatment plants, *Water research* 41(5) (2007) 1110-1120. <https://doi.org/10.1016/j.watres.2006.11.050>.
- [3] O. Sánchez, E. Aspé, M.C. Martí, M. Roedel, The Effect of Sodium Chloride on the Two-Step Kinetics of the Nitrifying Process, *Water environment research* 76(1) (2004) 73-80.
- [4] S. Judd, *The MBR book: principles and applications of membrane bioreactors for water and wastewater treatment*, second ed., Elsevier, Oxford, United Kingdom, 2010.
- [5] APHA. 1992. *Standard methods for the examination of water and wastewater*. 18th ed. American Public Health Association, Washington, DC.
- [6] F. Duarte, R. Gormaz, S. Natesan, Arbitrary Lagrangian–Eulerian method for Navier–Stokes equations with moving boundaries, *Computer Methods in Applied Mechanics and Engineering* 193(45-47) (2004) 4819-4836. <https://doi.org/10.1016/j.cma.2004.05.003>.
- [7] Z. Xu, F.M. Dehkordy, Y. Li, Y. Fan, T. Wang, Y. Huang, W. Zhou, Q. Dong, Y. Lei, M.D. Stuber, High-fidelity profiling and modeling of heterogeneity in wastewater systems using milli-electrode array (MEA): Toward high-efficiency and energy-saving operation, *Water Research* 165 (2019) 114971. <https://doi.org/10.1016/j.watres.2019.114971>.
- [8] D.R. Lide, *CRC handbook of chemistry and physics*, CRC press, Boca Raton, 2004.
- [9] U. Wiesmann, *Biological nitrogen removal from wastewater*, *Biotechnics/wastewater*, Springer1994, pp. 113-154.
- [10] L. Uby, Next steps in clean water oxygen transfer testing—A critical review of current standards, *Water research* 157(15) (2019) 415-434. <https://doi.org/doi.org/10.1016/j.watres.2019.03.063>.